Construction and Building Materials 521 (2026) 146102

Contents lists available at ScienceDirect

Construction and Building Materials

journal homepage: www.elsevier.com/locate/conbuildmat

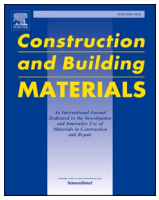

Optimized incorporation of shredded wind turbine blade waste in concrete using a particle packing approach

C. Duyal *, M. Chevalier, N. Lushnikova, F. Gauvin, H.J.H. Brouwers

Department of Built Environment Eindhoven University of Technology, P.P. Box 513, Eindhoven 5600 MB, the Netherlands

ARTICLE INFO

Keywords:
Wind turbine blade waste
Modified Andreasen and Andersen (A&A) model
Fiber reinforced concrete
Fracture characteristics
Alkali-silica reaction

ABSTRACT

The sustainable management of end-of-life wind turbine blades (WTB) represents a critical environmental challenge due to their complex composite structure and non-biodegradable nature. This study investigates the incorporation of shredded wind turbine blade (SWTB) waste into concrete as a multifunctional component. By utilizing the particle size distribution of SWTB (0.063–80 mm), the waste was integrated to simultaneously function as a partial cement replacement, aggregate substitute, and fiber reinforcement. A particle packing-based mix design approach using the Modified Andreasen and Andersen (MAA) model was employed to optimize the concrete skeleton. Four mixtures with SWTB contents of 0%, 1%, 3%, and 5% by total mass were evaluated. Experimental results demonstrate that while SWTB increases water and superplasticizer demand, the optimized packing structure maintains high mechanical performance, with 28-day compressive strengths exceeding 45 MPa. Even at the highest replacement level, this structural-grade performance was achieved alongside a simultaneous replacement of 10.2% vol. aggregate, 4.4% vol. cement, and 2.6% vol. fiber. Isothermal calorimetry revealed that epoxy residues do not retard hydration, while the fibrous fraction provided a significant toughening mechanism, increasing residual flexural strength by up to 250%. Durability assessments confirmed that SWTB does not trigger alkali-silica reactions (ASR). The findings suggest that the proposed design approach enables high-volume valorization of SWTB without compromising the structural integrity of the concrete, providing a scalable alternative to the landfilling of WTB waste.

1. Introduction

Concrete is a fundamental construction material and ranks second only to water in terms of global usage, with annual consumption close to 30 billion tonnes and global demand expected to increase by nearly 50% by 2050 [1,2]. Moreover, concrete production typically relies on a volumetric distribution of approximately 15% cement, 63% natural aggregates and 22% water, the demand for which is substantial [3]. Cement production is responsible for approximately 7–8% of global anthropogenic CO_2 emissions [4–6]. In addition, natural aggregates constitute approximately 60–80% of the total volume of concrete. In 2015, approximately 48.3 billion tonnes of natural aggregates were consumed worldwide and the every 5-year growth was estimated as more than 5% [7,8].

Several studies have focused on identifying alternative materials that can be used as cement and aggregate replacements to reduce the environmental impact of concrete [9,10]. One of the most widely studied approaches involves the incorporation of various waste materials into concrete. Islam et al. (2022) [11], studied the use of waste polypropylene as an aggregate replacement in concrete and found that aggregate replacement levels of up to 10% by volume can be considered feasible for the production of eco-efficient concrete. Yıldızel et al. (2023) [12], used waste tyres as fiber reinforcement in concrete and reported enhanced ductility. Zepper et al. (2024) [13], developed an approach for quantifying the main phases of basic oxygen furnace (BOF) slag to support its high-end utilization as a cement alternative. Taha and Alnahhal (2025) [14], investigated the combined use of recycled concrete aggregates and recycled concrete powder in concrete together with basalt fibers and ground granulated blast furnace slag. Their results demonstrated that optimized mix proportioning can enhance mechanical performance and durability when waste materials are incorporated into concrete.

Wind energy is a widely adopted sustainable energy source; however, wind turbine blades (WTB) typically have a service life of around 20 years. Following their end-of-life (EoL), WTBs are commonly incinerated or landfilled [15,16]. Considering that the first wind farms were

* Corresponding author.
E-mail address: c.duyal@tue.nl (C. Duyal).

https://doi.org/10.1016/j.conbuildmat.2026.146102
Received 6 January 2026; Received in revised form 10 March 2026; Accepted 22 March 2026
Available online 25 March 2026

built in the 1990s, the WTB waste stream is expected to increase significantly in the coming years. Annual global WTB waste is projected to reach approximately 200,000 tonnes by 2033 and 500,000 tonnes by 2050, with Europe contributing about 325,000 tonnes per year by 2050; cumulatively, total WTB waste is expected to amount to around 43.4 million tonnes worldwide by that time [17–19]. This situation increases the need for recycling and repurposing EoL WTBs. While reuse of whole wind turbine blades is not possible due to design constraints, certain blade components or size-reduced waste composites may be reused [20].

Modern wind turbine blades consist of composite materials, especially glass or carbon fiber reinforced polymers (GFRP, CFRP), with fibers embedded in a resin matrix at volume fractions of 12–60%. Their composite nature makes recycling challenging, and although thermal and chemical methods have been explored, they are not yet viable at an industrial scale [20,21]. Mechanical recycling offers an alternative route for waste WTB valorization, with being the most widely applied method owing to its energy efficiency and low cost. However, mechanical recycling produces outputs with a wide range of particle sizes and shapes. In addition, the resulting material contains both organic and inorganic compounds within its structure [22–24].

The incorporation of EoL WTBs into concrete offers dual benefits. It contributes to mitigating the environmental impacts associated with the landfilling of waste WTBs, and it enables a reduction in the ecological footprint of concrete through the partial replacement of its constituents, such as cement, aggregates, and fibers [25]. Many researchers have investigated the use of mechanically recycled WTBs in concrete in different roles. Tao et al. [24] categorized these roles based on replacement and reinforcement concepts.

Mechanical recycling of WTBs is commonly carried out using methods such as cutting, grinding, shredding, and crushing. Selective methods, particularly cutting, allow for the production of particles with more controlled sizes and morphologies. Yazdanbakhsh et al. [26] et al. used needle-shaped cut WTBs as aggregates in concrete and reported strength loss but improvement in toughness. In addition, Hofmeister [27] and Baturkin et al. [25] incorporated cut, cube-shaped WTBs as coarse aggregate replacements in concrete and reported compressive strength reductions in concrete of approximately 26% and 50%, respectively. Revilla-Cuesta et al. [28], selectively crushed the WTBs to achieve fibrous output. They used the WTB waste up to 6% by total concrete volume and observed a strength reduction at the highest dose of WTB use only. Fu et al. [29] produced macro fibers by cutting the wind turbine blade waste to have same length fibers to incorporate in concrete. They observed that increasing the fiber content to 1.5% resulted in a 30% increase in flexural strength.

Selective recycling of WTBs has been reported to be time-consuming and labor-intensive [29,30]. Therefore, non-selective mechanical recycling is more widely applied and involves size reduction through shredding without control over particle size or shape, resulting in a mixed output of flakes, fibers, and fine powder. The operational simplicity of the process, its relatively low energy demand, and its ability to efficiently recycle large volumes of waste within a short period make non-selective shredding more widely adopted than other alternative recycling methods for WTBs. Such recycling products are described in the literature as WTB fiber fluff, fiber clusters, or fiber–powder mixtures [30–32]. Shredded wind turbine blade waste (SWTB) is widely incorporated into concrete in various roles depending on its size and morphology, and sieving is commonly employed after shredding to classify the material into specific fractions. It has been reported that the fibrous fractions of SWTB enhance split tensile and flexural strength, improve the ductility of mortar and concrete, and reduce shrinkage and ASR-related cracking [24], [33–37]. Powder SWTB has also been investigated as a cement replacement, filler, and sand substitute in the literature. At replacement levels of approximately 5%, powdered SWTB used as a filler in mortar has been reported to have only a marginal influence on strength. At higher dosages, increased water demand leads to reduced workability. While high levels of cement replacement with SWTB tend to reduce strength by lowering the clinker content, limited replacement levels may contribute to hydration due to the Si- and Al-rich phases present in SWTB [25], [38–40].

This study aims to utilize SWTB, which exhibits a wide variety of shapes and sizes, by enabling different size fractions to simultaneously assume multiple roles within concrete. This multipurpose use refers to the ability of SWTB to function concurrently as aggregate replacement, cement replacement, and fiber reinforcement due to its size and morphological diversity. The concrete mixtures were designed with SWTB contents of 0% 1%, 3%, and 5% by total concrete mass. Within these mixtures, SWTB simultaneously acted as aggregate replacement at volume fractions of 0%, 2.6%, 6.2%, and 10.2%, as cement replacement at 0%, 0.9%, 2.6%, and 4.4%, and as fiber reinforcement at 0%, 0.5%, 1.6%, and 2.6%. In order to mitigate potential losses in performance associated with SWTB incorporation, a particle packing–based mix design approach was adopted in this study. The Modified Andreasen and

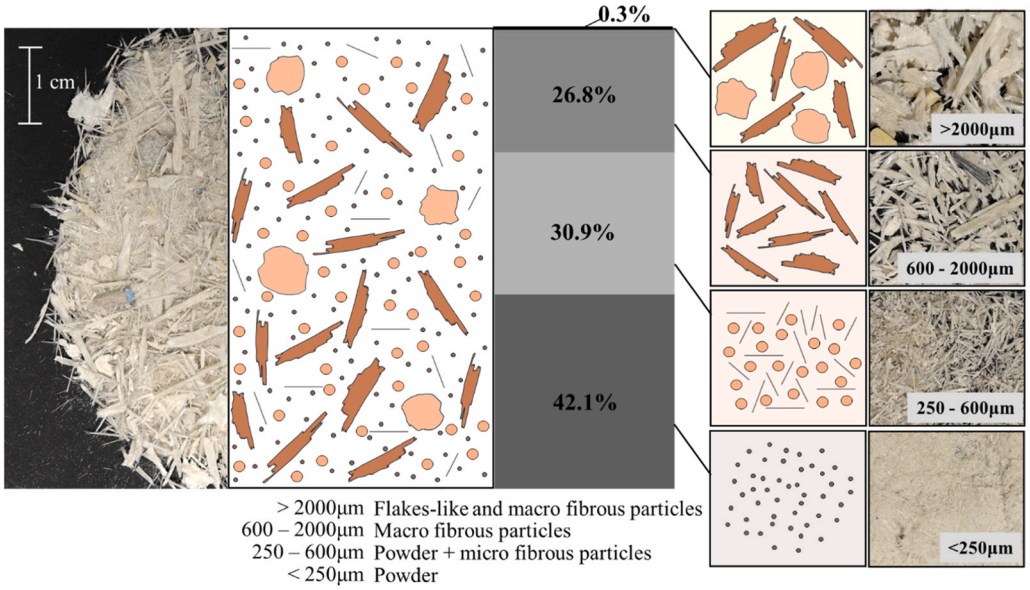

Fig. 1. Particle size distribution and schematic illustration of the shape characteristics of SWTB.

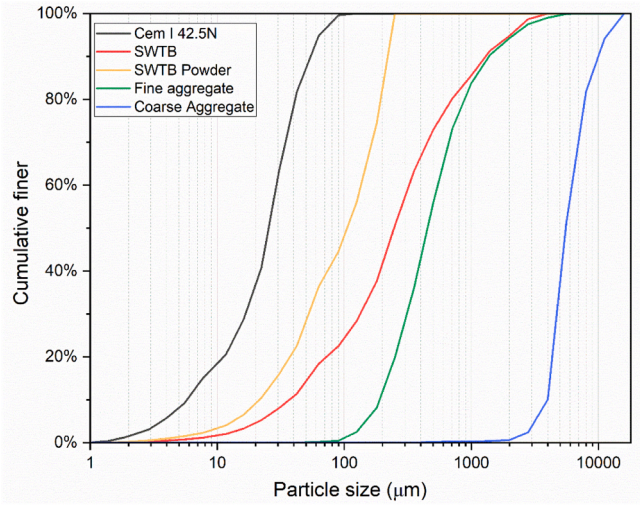

Fig. 2. PSD of raw materials.

Andersen (MAA) model, which is commonly used in high-performance concrete design [41–43], was applied to optimize the particle size distribution of the mixtures. This approach aimed to achieve a dense packing structure with low porosity, thereby helping to maintain the mechanical performance of concrete despite the high total SWTB content. The concrete mixtures were evaluated to assess the overall effects of SWTB in its different functional roles within concrete. The influence of SWTB used as a cement replacement was examined through hydration heat release and paste strength measurements. Fresh and hardened concrete properties were evaluated to assess the overall impact of SWTB. The mechanical and fracture performance of concrete were also examined to clarify the contribution of SWTB when acting as fiber reinforcement and aggregate replacement. Like other GFRP wastes, the use of SWTB in concrete may pose a risk of alkali–silica reaction (ASR) due to its high glass content [44]. The durability performance of the concretes were evaluated through drying shrinkage measurements for 120 days and ASR testing. Microstructural examinations were performed on the specimens.

2. Raw materials

In this study, SWTB obtained from Spain (PreZero Gestion De Residuos SA) was used. The material originates from mechanical recycling of WTB waste. The EoL WTBs were first subjected to a pre-treatment process to remove wooden components present in the internal structure. Subsequently, the blades were cut into smaller sections. The cut blade segments were then transported via automated conveyor belts to an industrial shredder, where a non-selective mechanical shredding process was applied. During this process, SWTB particles with various sizes and irregular shapes were generated. After shredding, the material passed along a conveyor belt equipped with magnetic separation to remove potential metallic residues originating from internal blade components. At the end of this process, the final SWTB was collected. The particle size of received SWTB ranges from 0.063 mm to 80 mm.

Cem I 42.5 N, supplied by Heidelberg Benelux (the Netherlands), was used as the binder. Natural river gravel and river sand were used as coarse and fine aggregates, respectively, both sourced from the Netherlands. The sand has a particle size range of 0.075– 4.6 mm, while the gravel ranges from 8 to 16 mm. The superplasticizer used in this study was Sika ViscoFlow−37, supplied by Sika Belgium, to reach an adequate workability.

Table 1
Physical properties of raw materials.

Materials	Specific Density (g/cm^3)	Water Absorbtion (%)	pH
Cem I 42,5 N	3.15	-	-
SWTB	1.79	22.97	7 ± 1
Fine aggregate	2.65	2.61	-
Coarse aggregate	2.68	1.22	-
Superplasticizer	1.07	-	5 ± 1

Table 2
Aspect ratios of the fibrous SWTB fraction across different size groups.

Fibrous SWTB fraction	> 2000 μm	600 – 2000 μm	250 – 600 μm
Aspect ratio	16.60	17	23.70
Length (mm)	10.70	6.50	0.45
Cross Sectional length (mm)	1.04	0.51	0.02

2.1. Particle size distribution, aspect ratio, water absorption and density

Laser diffraction (Fritsch Analysette 22) was used to determine the particle size distribution (PSD) of the fines: cement and the powder fraction of SWTB. The PSD of the coarser fractions was determined according to EN 933–2 [45] using a set of sieves, with a $\sqrt{2}$ ratio selected between sieve sizes. Particle size distribution and schematic illustration of the shape characteristics of SWTB is given in Fig. 1. Because of the heterogeneous particle shape of SWTB, optical microscopy combined with ImageJ software was used in addition to PSD analysis to determine the length and aspect ratio of the fibrous particles. The aspect ratios of the fibrous SWTB fractions were measured for fibers across different size ranges. The particle size distribution of all raw materials is given in Fig. 2. The water absorption of SWTB and natural aggregates was measured in accordance with EN 1097–6 [46], while the specific density of SWTB was determined using a helium pycnometer (AccuPyc II 1340). SWTB has a density of 1.79 g/cm^3 and a water absorption of 22.97%. For the natural aggregates, the supplier provided the density values, while water absorption was determined in the same way as for SWTB. Physical properties of raw materials are given in Table 1. The average aspect ratio of fibrous SWTB was found to be around 19. Table 2 presents the aspect ratios of the fibrous SWTB fraction across different size groups.

2.2. Chemical composition

The compositions of cement and SWTB were analyzed using an XRF spectrometer (PANalytical Epsilon 3 range) on fused beads. Prior to the analysis, the samples were finely milled, and the loss on ignition (LOI) was determined by heating them to 950 °C for 1 h. It can be seen that SWTB mainly consists of SiO_2 (38.33 wt%), CaO (16.85 wt%), and Al_2O_3 (11.12 wt%). While these three components represent the majority of the composition, the LOI at 950 °C was 31.7 wt%, indicating the high amount of organic material in SWTB. The organic fraction was further analyzed using thermogravimetric analysis (TGA) under a nitrogen (N_2) atmosphere over a temperature range of 20–850 °C and with FTIR (Perkin Elmer). According to the TGA results, the major decomposition of SWTB occurred between 310 °C and 420 °C. FTIR analysis revealed characteristic absorption peaks at approximately 1250 cm^{-1}, corresponding to C–O–C stretching vibrations, and around 1500 cm^{-1}, associated with aromatic C=C bonds. These bonds are indicative of epoxy resin, confirming that epoxy is the main organic component of the SWTB [47]. Chemical composition of raw materials can be seen in Table 3.

2.3. Concrete mix design

In this study, SWTB was incorporated into concrete without additional sorting or sieving, thereby utilizing its full range of particle sizes and shapes as a multipurpose component (Fig. 1). The overall mix design

Table 3
Chemical composition raw materials (unit: %wt.).

	CaO	SiO_2	Al_2O_3	Fe_2O_3	MgO	SO_3	K_2O	Rest	LOI
CEM I 42,5 N	67.86	14.75	3.60	3.13	1.38	4.46	0.82	1.77	2.16
SWTB	16.85	38.33	11.12	1.16	-	-	-	0.82	31.70

*LOI= Loss on ignition at 950°C

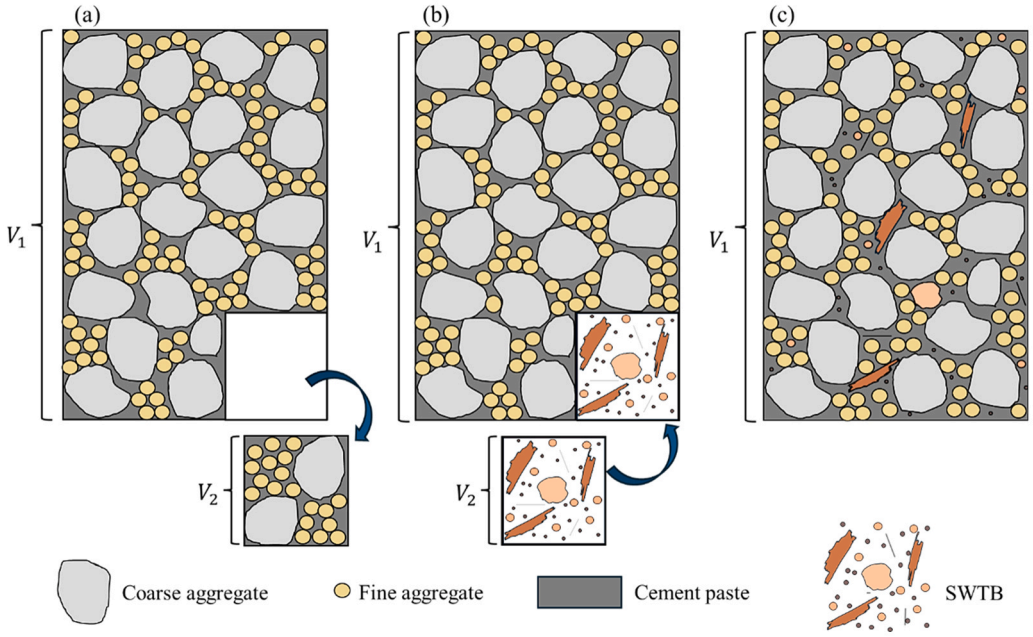

Fig. 3. Schematic illustration of the concrete design approach. V_1 represents the total concrete volume, and V_2 denotes the portion selected for replacement. (a) Reference concrete with the predefined replacement volume (V_2) indicated, (b) SWTB fractions occupying the replacement volume, and (c) Concrete incorporating SWTB, where particles function in multiple functional roles.

strategy followed three main steps: applying the MAA model, accounting for the fibrous fraction in the mix calculations, and adjusting the water content to maintain a target water/cement ratio of 0.4, in accordance with the American Concrete Institute (ACI) design method.

The MAA method was used to design the packing of the powder and granular fractions, ensuring improved density and reduced porosity [41, 42]. The fibrous fraction, although not physically added separately, was treated in the calculations as a distinct fiber addition to capture its reinforcing role in the composite. Finally, due to the high water absorption of SWTB, the effective water content of the mixtures was adjusted following the ACI mix design method [48].

Through this combined approach, SWTB particles could act as cement replacement, fine and coarse aggregate replacement, and fiber reinforcement, depending on their size and shape. The main concept of the mix design strategy is the replacement of a portion of the concrete volume with SWTB. This approach is schematically illustrated in Fig. 3.

Four concrete mixes were designed to evaluate the influence of SWTB on concrete properties. All mixes were proportioned following the same design methodology to ensure consistency and comparability of the results. The SWTB contents of the designed concrete mixes were set at 0%, 1%, 3%, and 5% by total concrete mass. The concrete was designed to match the target curve of the Modified Andreasen and Andersen (MAA) model [49]:

$$P_{target}\left(D_i^{i+1}\right) = \frac{\left(D_i^{i+1}\right)^q - D_{\min}^q}{D_{\max}^q - D_{\min}^q} \tag{1}$$

where D_{min} and D_{max} represent the minimum and maximum particle size and q is the particle size distribution modulus. In the MAA method, the distribution modulus governs the workability of the mix. The target slump was set to consistency class S3. For vibrated concrete, the q value is typically around 0.35. However, Hüsken and Brouwers [50] reported that higher q values tend to decrease the average packing density. To mitigate potential workability loss associated with the incorporation of SWTB, various q values were empirically tested. Ultimately, $q = 0.25$ was selected as an optimal value, maintaining adequate workability while avoiding a reduction in packing density. Once the target composition is determined, the mix composition can be calculated by:

$$P_{mix}\left(D_i^{i+1}\right) = \sum_{j=1}^{n} \alpha_j * D_i^{i+1} \tag{2}$$

where, n is the number of the fines and aggregates used in the concrete composition. $\forall j \in [1; n]$, α_j is the proportion of the j^{th} component in the mix. The α_j are the variables to determine. Afterwards, the residual sum of squares (RSS) and the coefficient of determination (R^2), which quantifies the fitting degree between the target and actual packing curves are calculated. A denser particle packing structure is achieved when R^2 approaches to 1, indicating a strong agreement between the target and actual packing curves [51].

A Python program developed by the author that computes the proportions α_i, $\forall i \in [1;n]$ that minimize the R^2. To execute the program, the initial bounds for the material proportions need to be set. Their sum must equal 100%, and each individual proportion should lie within the range of 0–100%, as expressed by:

$$\forall i \in [1;n], \quad \alpha_i \in [0\%;100\%] \; and \; \sum_{i=1}^{n} \alpha_i = 100\% \tag{3}$$

The target and mix curves of the granular concrete mix design are

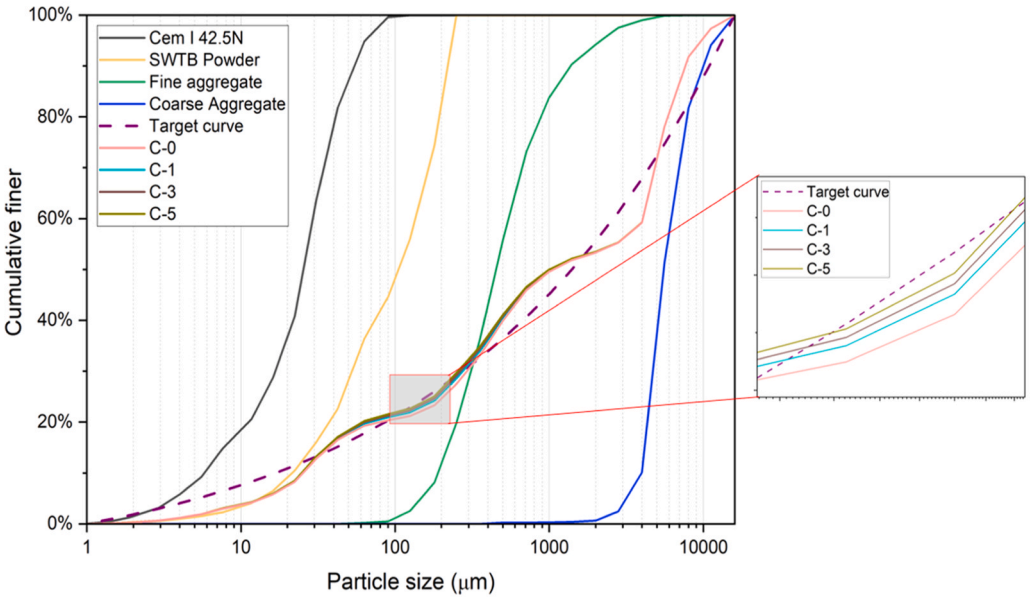

Fig. 4. Target curve, granular components, and resulting mix curves for the initial stage of the concrete design.

Table 4
Concrete recipes for 0%, 1%, 3% and 5% of SWTB for 1 m^3 concrete (unit: kg).

	C−0	C−1	C−3	C−5
Cem I 42.5 N	503.20	496.50	483.50	470.90
Fine aggregate (sand)	740.80	717.70	672.60	628.50
Coarse aggregate (gravel)	963.20	951.20	927.80	905.00
SWTB	0.00	24.00	70.70	116.50
Superplasticizer (SP)	0.06	0.07	0.13	0.16
Water	201.30	203.20	206.80	210.40

shown in Fig. 4.

The program provided optimized proportions for each component after execution. However, the algorithm provided the results in terms of apparent volume. Since concrete mixtures are typically prepared by weight, where mass-based measurements are more accurate and practical, these proportions were converted to mass values. This was achieved by multiplying each volume fraction by the specific density of the corresponding material, as shown by [51]:

$$\forall i \in [1;n], \quad m_i = \alpha_i * \rho_i^{app} \tag{4}$$

where, m_i is the mass amount and, the ρ_i^{app} is the apparent density of material.

Once the granular fractions were optimized, the fibrous fraction of SWTB was incorporated into the mix design. To ensure consistency, additional constraints were applied, such as defining minimum or maximum allowable proportions for certain components. For SWTB, the total content was fixed at 0%, 1%, 3%, and 5% of the total concrete mass, and the mixes were denoted as C−0, C−1, C−3, and C−5, respectively. The designed concrete mix proportions are presented in Table 4. Within this range, about 10% of the SWTB particles were of a suitable size for cement replacement; however, the actual cement replacement was restricted to a maximum of 2.5% by mass. The remaining fine fraction was incorporated as a micro-filler, contributing to the overall packing density. These constraints were embedded in the program, which iteratively adjusted the proportions until all requirements were met. A schematic representation of workflow is presented in Fig. 5.

As SWTB acts as a multifunctional component in the mixtures, its replacement and reinforcement levels are summarized in Table 5. The quantitative allocation of SWTB among cement replacement, aggregate substitution, and fiber reinforcement was first established for the mixture with the highest SWTB dosage (C−5), representing the maximum incorporation level investigated in this study. This mixture was used as the reference case to define the role-based distribution of SWTB according to its particle size distribution (PSD) and morphological characteristics, before proportionally scaling the same distribution to the remaining mixtures.

Particle size distribution analysis indicated that approximately 20% of the total SWTB mass fell within the particle size range suitable for cement replacement. However, utilizing the entire cement-sized fraction as a binder substitute would have resulted in a relatively high level of cement substitution, which may affect performance. Therefore, cement substitution was intentionally limited to a maximum of 2.5% by mass of cement. Under this constraint, only 10.5% of the total incorporated SWTB in mixture C−5 was assigned to the cement replacement role. The corresponding volumetric contribution was calculated by converting this mass fraction into volume using the measured specific density of SWTB (1.79 g/cm^3) and normalizing it with respect to the total concrete volume (1 m^3).

Once the cement replacement level was established, the remaining SWTB was allocated to aggregate substitution based on its size fractions. The corresponding aggregate substitution proportions were determined using the Python program applied in the mix design. Approximately 58% of SWTB fell within the sand-sized fraction, while about 22% corresponded to the coarse aggregate range. Their volumetric contributions were determined by converting the respective SWTB masses into volume and expressing them relative to the total concrete volume.

In parallel, morphological analysis showed that approximately 40% of the total SWTB mass consisted of elongated particles with an average aspect ratio of about 19. This fibrous portion was quantified independently by converting the corresponding mass into volume and normalizing it to the total concrete volume. Since fibrous particles are distributed across multiple size intervals, the reinforcement fraction may partially overlap with the size-based aggregate fractions and is therefore reported separately as a morphology-based reinforcement indicator.

Once the functional distribution was defined for C−5 mix, the corresponding replacement and reinforcement levels in mixtures C−1 and C−3 were obtained by proportional scaling of the total SWTB content while maintaining the same relative allocation among functional roles. The reference mixture C−0 contained no SWTB and served as the

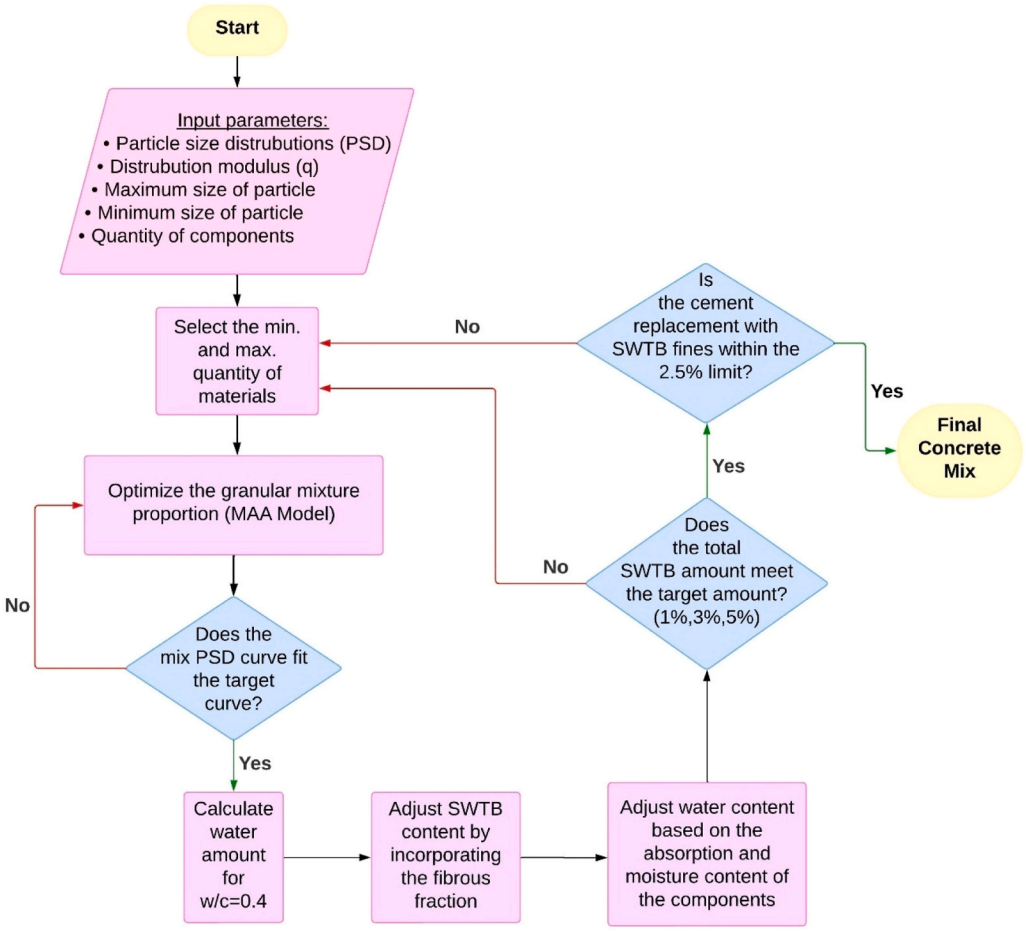

Fig. 5. Workflow of the overall concrete mix design.

Table 5
Total incorporation of SWTB in concrete and its distribution according to functional roles.

Sample ID	Amount in total concrete			Amount per component	
	Used SWTB (mass %)	Used SWTB (vol%)	Fiber reinforcement (vol%)	Aggregate replacement (vol%)	Cement replacement (vol%)
C−0	0.0	0.0	0.0	0.0	0.0
C−1	1.0	1.0	0.5	2.1	0.9
C−3	3.0	4.0	1.6	6.2	2.6
C−5	5.0	7.0	2.6	10.2	4.4

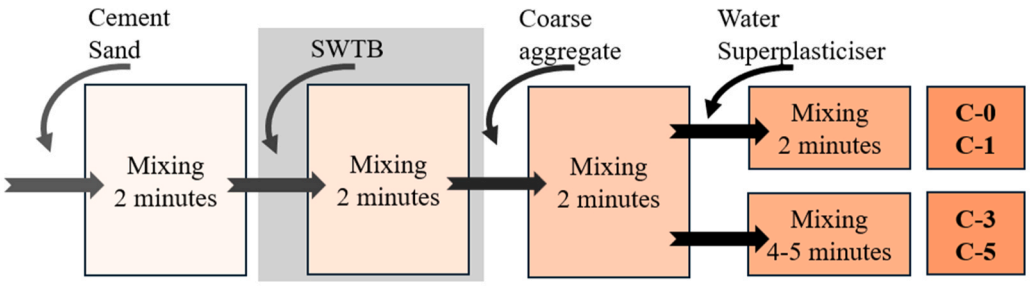

Fig. 6. Mixing procedure of concrete.

baseline for comparison.

2.4. Mixing procedure and sample fabrication

The mixing procedure has a significant influence on the fresh and hardened properties of concrete, particularly when incorporating SWTB.

Table 6
Prepared samples and their abbreviations.

SWTB in concrete (% mass)	Concrete	Mortar	Cement Paste
0	C−0	M−0	P−0
1	C−1	M−1	P−1
3	C−3	M−3	P−3
5	C−5	M−5	P−5

Table 7
Designed paste samples (unit: g).

Component	P−0	P−1	P−3	P−5
Cem I 42.5 N	100.0	99.5	98.5	97.5
SWTB powder	0	0.5	1.5	2.5
Water	40	40	40	40

Table 8
Mix designs of mortar samples for accelerated mortar bar test (unit: g).

Component	M−0	M−1	M−3	M−5
Cem I 42.5 N	549	546	543	541
Fine aggregate (Sand)	1235	1217	1186	1156
SWTB	0	12	37	61
Water	258	257	255	254

Due to its heterogeneous morphology, including elongated fibrous particles and epoxy-rich polymeric surfaces, SWTB may form localized clusters during mixing. The hydrophobic nature and relatively low surface energy of the epoxy further enhance fiber–fiber interaction, facilitating agglomeration. To minimize this effect, SWTB was introduced during the dry-mixing stage to allow mechanical separation prior to water addition. Cement and sand were first dry mixed, followed by the addition of SWTB. Coarse aggregate was then incorporated to further assist physical dispersion, and finally water and superplasticizer were added. Mixing time depended on the SWTB content. The overall procedure is summarized in Fig. 6.

Following the mixing process, specimens were cast in two different types molds for each recipe. Cubic molds (150 × 150 × 150 mm^3) were utilized for compressive and splitting tensile strength testing. Simultaneously, prismatic molds (100 × 100 × 500 mm^3) were prepared to evaluate the elastic modulus, flexural performance with three-point bending test, crack mouth opening displacement (CMOD), and drying shrinkage. The selected mold dimensions comply with the standards recommended for fiber-reinforced concrete (FRC) testing [52]. Before casting the specimens, a slump test was performed in accordance with ASTM C143 [53] to evaluate the effect of SWTB incorporation on concrete workability. After casting, the samples were kept in their molds for 2 days to limit early moisture loss and ensure stable initial hydration. Subsequently, specimens designated for mechanical testing were cured in water at 20 ± 2 °C until the testing ages of 7 and 28 days. Shrinkage measurements were initiated immediately after demolding.

2.5. Testing methods of concrete, cement paste and mortar

The multifunctional behavior of SWTB was evaluated through fresh property, mechanical performance, and durability tests on concrete, cement paste, and mortar to assess its simultaneous roles as cement replacement, aggregate substitution, and fiber reinforcement. Prepared samples and their abbreviations can be seen in the Table 6. To represent the concrete mixtures with 0%, 1%, 3%, and 5% SWTB by mass, corresponding cement paste samples were prepared and labeled as P−0, P−1, P−3, and P−5. The cement replacement levels in these pastes were 0.0%, 0.5%, 1.5%, and 2.5% by mass, respectively. Mortar samples with

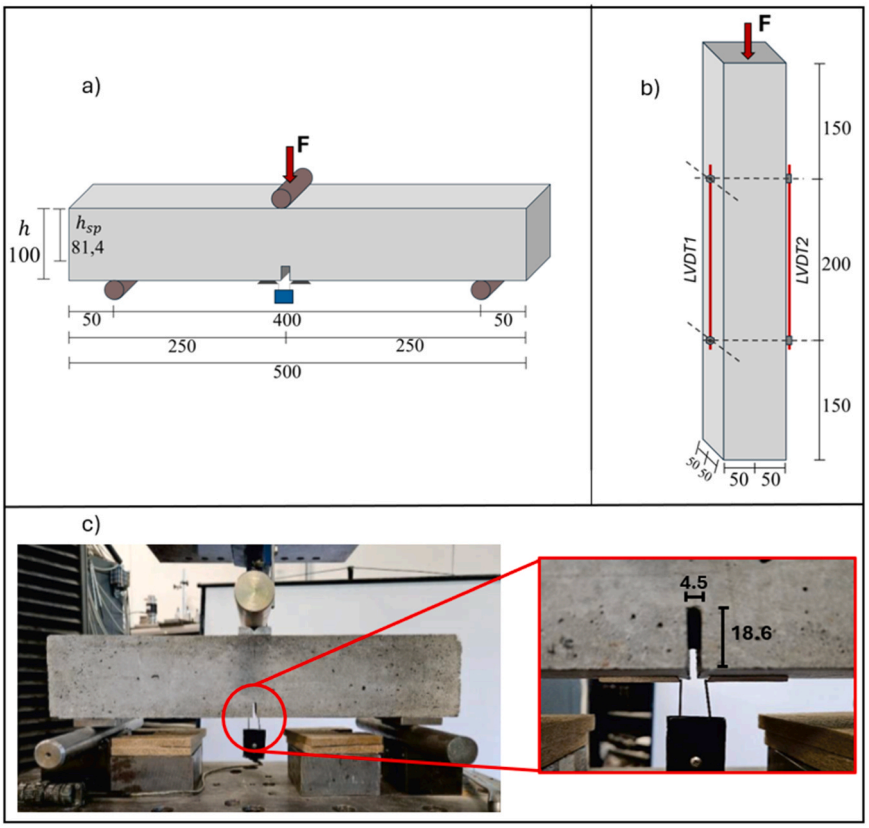

Fig. 7. Experimental setups (dimensions in mm): (a) CMOD test setup, (b) EMod test setup, and (c) concrete specimen with a preformed notch and clip gauge for the CMOD test.

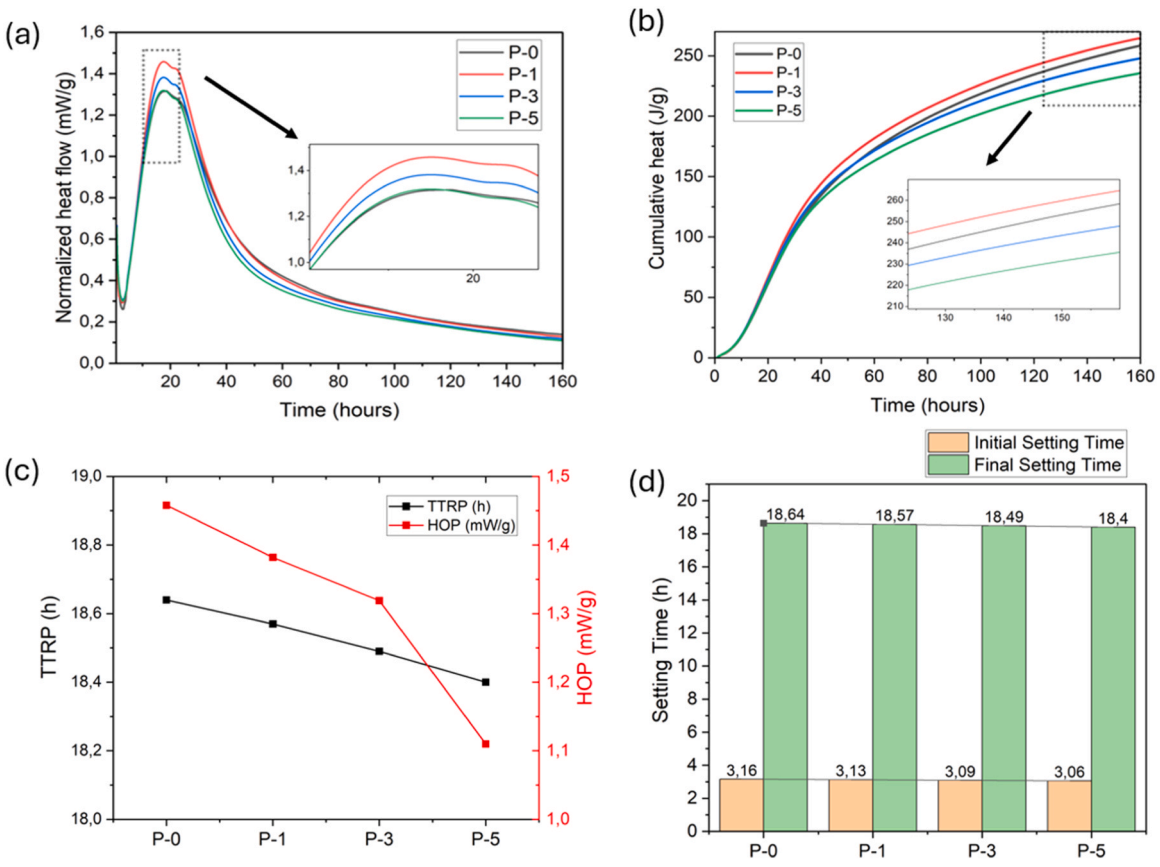

Fig. 8. Calorimeter data showing (a) Normalized heat flow; (b) Normalized total heat release; (c) Time to reaction peak (TTRP) and normalized height of peak (HOP); (d) Initial and final setting time.

0%, 1%, 3%, and 5% SWTB by mass, named M−0, M−1, M−3, and M−5, were prepared to evaluate alkali–silica reactivity (ASR). The mix proportions of the cement paste and mortar samples are given in Table 7 and Table 8, respectively. Designed concrete recipe is given in the Table 4.

2.6. Mechanical tests

The compressive strength (*fc*) was measured on 150 mm cubic specimens at 7 and 28 days. Curing conditions followed EN 12390–2 [54], while compressive testing was carried out in accordance with EN 12390–3 [55] at a constant loading rate of 10 kN/s. The splitting tensile strength (*fct*) was determined in accordance with EN 12390–6 [56]. Prior to testing, each specimen was prepared with two hardboard packing strips, as specified in the standard.

CMOD test was conducted on prismatic concrete specimens at 28 days of curing, using a three-point bending configuration in accordance with EN 14651 [57]. For the CMOD test, a central notch was cut at the bottom of each specimen, measuring 4.5 mm in width and 18.6 mm in depth. A clip gauge was then attached at the notch mouth to record crack opening during the three-point bending test. The flexural tensile strength (f_R) was also determined from the CMOD test using:

$$f_R = \frac{3Fl}{2bh_{sp}^2} \tag{5}$$

where F is the applied load, l is the span length, b is the specimen width, and h_{sp} is the distance between the notch tip and the top of the specimen.

The secant modulus of elasticity (EMod) was determined in compression according to EN 12390–13 [58]. Testing was performed on 100 × 100 × 500 mm³ prisms with the compressive load applied to the 100 × 100 mm² faces. To minimize boundary effects, axial strain was recorded at the mid-height of the specimen using two LVDTs with a 200 mm gauge length. Repeated loading cycles were applied as specified in the standard, with a 10 kN preload stress (σ_p) and a lower stress limit defined as $\sigma_a = f_c/3$. The EMod was calculated using:

$$E = \frac{\Delta\sigma}{\Delta\varepsilon} = \frac{\sigma_a - \sigma_p}{\varepsilon_{a,3} - \varepsilon_{p,2}} \tag{6}$$

where $\varepsilon_{a,3}$ and $\varepsilon_{p,2}$ represent the deformations measured by the LVDTs at the third and second plateaus of the repeated load cycles, corresponding to stresses σ_a and σ_p, respectively. Fig. 7 provides a schematic representation of the CMOD controlled bending and EMod test setups.

Cement paste specimens were prepared in 25 × 25 × 25 mm³ cubic molds, and their 28-day compressive strength was measured.

2.7. Shrinkage

The free drying shrinkage of concrete prisms was measured in accordance with EN 12390–16 [59] under drying conditions at 20 ± 2 °C and 60 ± 2% relative humidity. Measurements were initiated immediately after demolding, without prior water curing, to capture the early-age drying response. Length changes were recorded using gauge studs fixed to the four longitudinal faces of the prismatic concrete specimens and measured with a three-digit sensitive gauge. Measurements were conducted over a period of 120 days on a logarithmic time scale.

2.8. Alkali silica reactivity testing

The potential for alkali–silica reaction (ASR) was evaluated in accordance with ASTM C1260 using the accelerated mortar bar test [60]

on produced mortar specimens (Table 8). After initial curing, mortar bars were immersed in a 1 N NaOH solution at 80 °C. Their length change was monitored over a 14-day period using a three-digit sensitive gauge.

2.9. Isothermal calorimetry

The cement paste of the concrete was investigated using paste samples prepared according to the mixture proportions in Table 7. Heat evolution was monitored with an isothermal calorimeter (TAM Air). After a 5-minute mixing period, the pastes were placed in the sample containers, and heat flow and cumulative heat release were continuously recorded for 7 days (168 h). Since the calorimeter requires a short stabilization period, the first 45 min of data were excluded from the analysis.

2.10. SEM

Following the 28-day compressive strength tests, representative samples were collected from the C−5 concrete mixture. Similarly, specimens were obtained from the M−5 mortar mixture 90 days after the ASR tests to examine microstructural features. To preserve the pore structure, a low-viscosity epoxy resin was used to impregnate the capillary pores and voids. The samples were subsequently sectioned and polished for analysis. Microstructural characterization was performed using a Phenom ProX scanning electron microscope (SEM) equipped with energy-dispersive X-ray spectroscopy (EDS).

3. Results and discussion

3.1. Hydration process

The proportions for the SWTB cement substitute were determined based on the equivalent cement content within the concrete paste (Table 7) to ensure an accurate comparison of the hydration effects. The subsequent analysis of heat flow and cumulative heat release, presented in Fig. 8, characterizes the early-age reaction kinetics.

Fig. 8(a) presents the normalized heat flow curves of cement pastes containing different levels of SWTB powder replacement. For all mixtures, the main hydration peak associated with the acceleration period occurs between 10 and 20 h. An increase in SWTB content does not lead to any noticeable retardation in hydration kinetics. However, the magnified inset shows that mixtures with lower SWTB contents exhibit slightly higher heat flow values at the main hydration peak.

Fig. 8(b) displays the cumulative heat release over a 7-day period. An overall decline in total heat release was observed with increasing SWTB content, which is primarily attributable to the dilution effect [40]. Particularly after 120 h, the P−3 and P−5 mixes show lower cumulative heat relative to the reference paste. These results indicate that while SWTB powder does not chemically retard hydration, its role as a partial cement substitute reduces the overall reaction intensity due to the lower clinker content in the system. The resinous phase in SWTB is nonreactive in a cementitious environment, which reduces the effective binder content and limiting the supply of calcium ions required for the generation of C-S-H and other hydrates. While this lowers the total heat evolution, at lower replacement levels, the glassy phase of the SWTB powder appears to partially compensate for the dilution. This slight enhancement in early hydration aligns with the corresponding compressive strength results.

Fig. 8(c) illustrates the evolution of the time to reach the reaction peak (TTRP) and the normalized height of the hydration peak (HOP). While the TTRP remains relatively stable, showing only a minor decrease from 18.64 to 18.40 h with higher SWTB content, the HOP exhibits a more pronounced decline from 1.46 mW/g to 1.10 mW/g. This reduction is primarily attributed to the lower reactivity of SWTB compared to cement, which subsequently diminishes the overall hydration response [25].

Fig. 8(d) presents the setting time results derived from the isothermal calorimetry data [40,61]. The results indicate that increasing the SWTB powder content does not significantly influence either the initial or final setting times. The initial set occurs between 3.16 and 3.06 h, while the final set shows only a marginal change from 18.64 to 18.40 h. This behavior suggests that the epoxy residues in the SWTB powder do not impart a quantifiable delay in cement hydration.

Table 9
Fresh properties of concrete mixes with different SWTB contents.

Sample	Slump (mm)	Fresh Density (kg/dm^3)	Air content (%vol.)
C−0	175 ± 5	2.34 ± 0.02	3 ± 0.01
C−1	140 ± 3	2.33 ± 0.01	2.5 ± 0.01
C−3	57 ± 2	2.32 ± 0.02	1.6 ± 0.02
C−5	27 ± 2	2.28 ± 0.02	7. ± 0.01

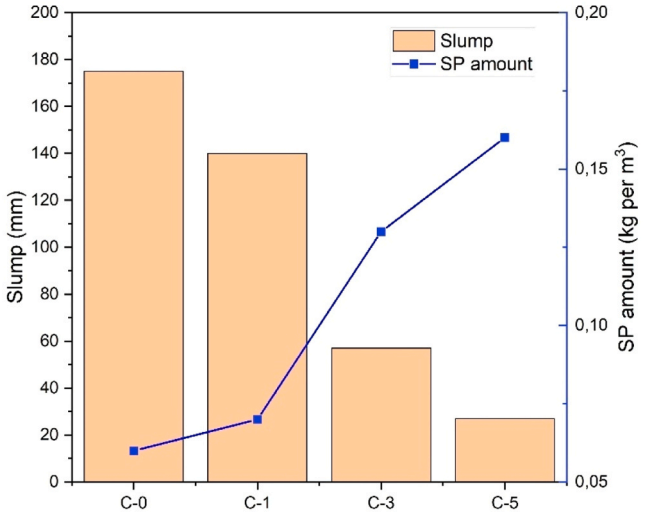

Fig. 9. Effect of SWTB content on slump and superplasticizer (SP) demand.

3.2. Workability

The workability of fresh concrete containing SWTB was evaluated by slump testing, with three measurements performed for each mix prior to casting. A consistent reduction in slump was observed with increasing SWTB content, a trend frequently reported in the literature [32,34,62]. This behavior is comparable to that of fiber-reinforced concrete, in which fibrous additions increase the total surface area and enhance the internal shear resistance of the mix. Consequently, the reduction in free water limits both lubrication and cement hydration, leading to a decrease in overall workability [30]. The irregular shape and high aspect ratio of the SWTB further promoted mechanical interlocking, intensifying the loss of workability. Although the superplasticizer dosage was adjusted during mixing, the reduction in slump remained evident. Beyond a certain dosage, the superplasticizer reached a saturation point and did not produce further improvement in workability. Moreover, the loss of workability associated with SWTB is largely attributed to mechanical interlocking and particle interaction, which cannot be fully compensated by additional chemical admixture.

Visual inspection confirmed that none of the mixes exhibited segregation or bleeding. The average slump values are presented in Table 9, and the relationship between superplasticizer (SP) demand, SWTB dosage, and slump is illustrated in Fig. 9.

The fresh density decreased slightly between the mixes with higher and lower SWTB contents. This reduction is attributed to the lower density of SWTB relative to other concrete components, as well as the

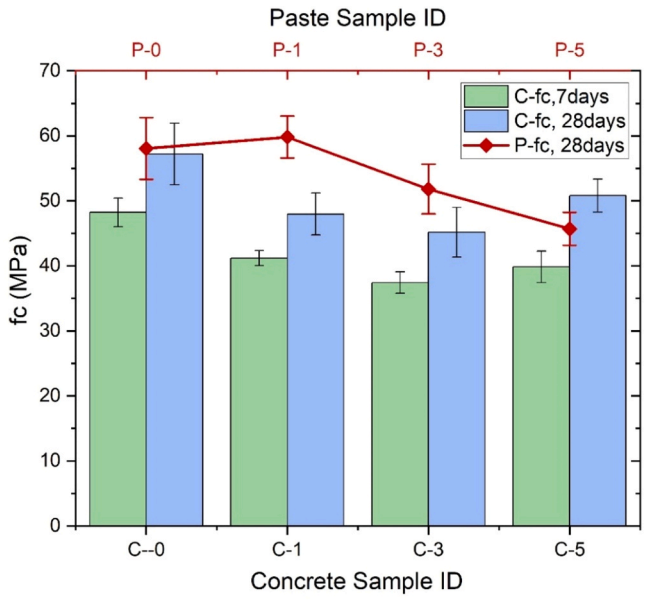

Fig. 10. Compressive strength of concrete samples at 7 and 28 days, and cement paste samples at 28 days.

higher water and admixture demands in mixtures with high SWTB dosages [28]. Simultaneously, the air content decreased as the SWTB dosage increased, which can be explained by the filler effect of the fine SWTB fractions resulting from the particle-packing-based mix design (Table 9).

3.3. Mechanical properties

In this subsection, the mechanical properties of the hardened concrete mixes are presented.

3.3.1. Strength

The compressive strength (f_c) of all concrete mixtures was evaluated at curing ages of 7 and 28 days. These results are presented in Fig. 10 and summarized in Table 10. A consistent trend was observed across all mixtures, with average compressive strengths exceeding 35 MPa at 7 days and 45 MPa at 28 days. While the reference mixture exhibited the highest strength, the inclusion of SWTB generally led to a strength reduction. Notably, the extent of this decrease became less pronounced at higher SWTB contents.

In contrast, an opposite trend was observed in the cement paste specimens. The 28-day compressive strengths of the pastes closely aligned with the calorimetric findings: partial replacement of cement with small amounts of SWTB powder resulted in a measurable increase in strength.

Despite the replacement of significant portions of both the aggregates (10.2%) and cement paste (2.5%) with SWTB, which exhibits lower load-bearing capacity and limited reactivity, the concrete mixtures maintained a high level of mechanical performance. The reference mixture reached an average 28-day compressive strength of 57.57 MPa, while the C−5 mixture achieved 51.3 MPa. This corresponds to a strength reduction of approximately 11%, indicating that the designed mixtures retained substantial compressive strength. This sustained performance can be attributed to the optimized mix design with a densely packing skeleton of concrete, resulting in a reduced porosity in the matrix [63].

The splitting tensile test results are summarized in Table 10 and

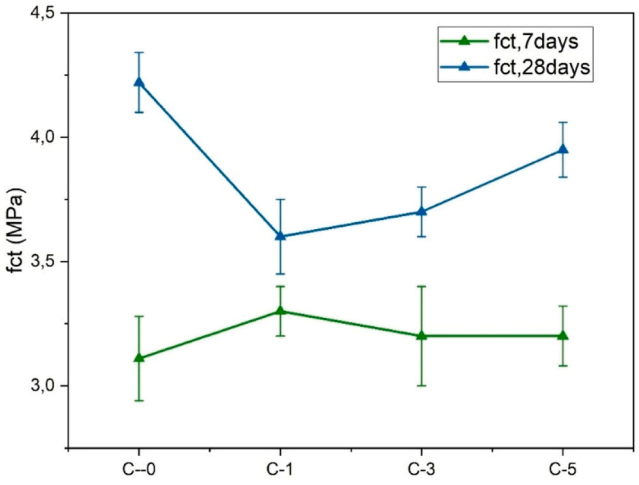

Fig. 11. Split tensile strength of concrete samples at 7 and 28 days.

Table 10
Mechanical properties of concrete samples.

Sample ID	Sample No	Compressive Strength (MPa)	Compressive Strength (MPa)	Split Tensile Strength (MPa)	Split Tensile Strength (MPa)	Flexural Strength (MPa)	Elastic Modulus (GPa)
		(7d)	(28d)	(7d)	(28d)	(28d)	(28d)
C−0	1	48.42	59.34	2.96	4.23	6.17	38.10
	2	50.37	59.73	3.11	4.35	5.94	40.20
	3	45.93	53.65	3.40	4.12	-	40.50
	Average	**48.24**	**57.57**	**3.16**	**4.23**	**6.06**	**39.60**
	St. Dev.	**2.23**	**3.40**	**0.22**	**0.12**	**0.16**	**1.31**
C−1	1	41.48	50.18	3.44	3.82	5.52	39.10
	2	39.92	46.86	3.16	3.67	5.46	36.80
	3	42.26	47.24	3.21	3.45	5.28	38.40
	Average	**41.22**	**48.09**	**3.27**	**3.65**	**5.42**	**38.10**
	St. Dev.	**1.19**	**1.82**	**0.15**	**0.19**	**0.12**	**1.18**
C−3	1	35.23	44.72	2.71	3.81	5.93	33.90
	2	36.56	44.36	3.32	3.95	5.81	36.50
	3	39.33	46.55	3.65	3.69	5.80	36.70
	Average	**37.04**	**45.21**	**3.23**	**3.82**	**5.85**	**35.70**
	St. Dev.	**2.09**	**1.17**	**0.48**	**0.13**	**0.07**	**1.56**
C−5	1	37.12	47.84	3.32	4.11	6.42	31.60
	2	41.35	52.73	3.03	3.83	6.21	32.00
	3	40.52	53.35	3.41	3.87	6.15	29.10
	Average	**39.66**	**51.31**	**3.25**	**3.94**	**6.26**	**30.90**
	St. Dev.	**2.24**	**3.02**	**0.20**	**0.15**	**0.14**	**1.57**

*Flexural strength values for C−0 are based on two tested specimens.

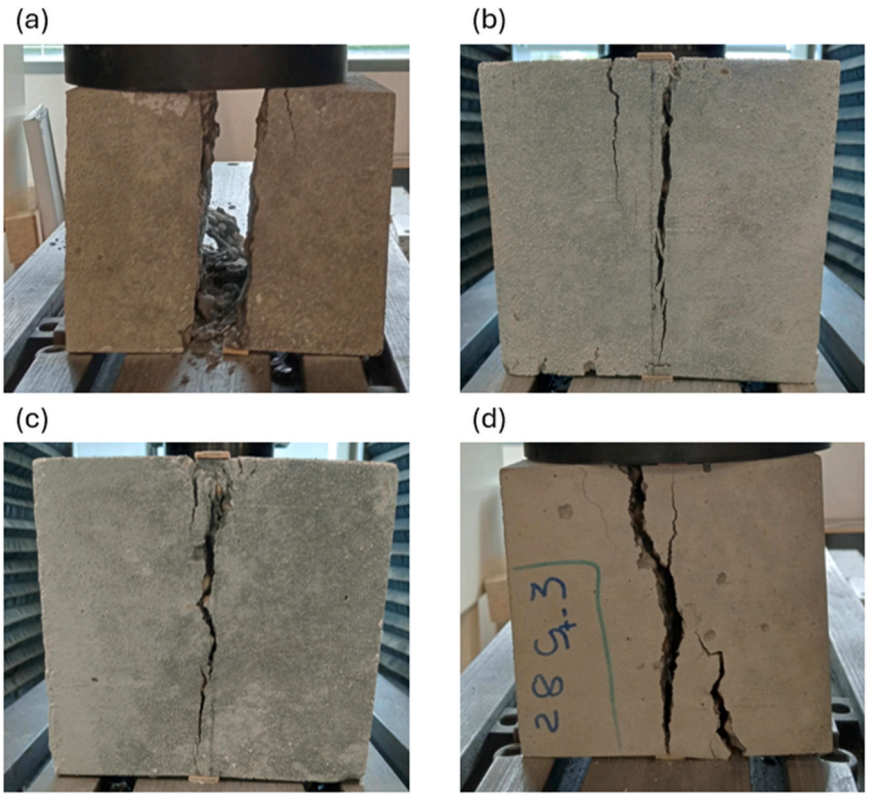

Fig. 12. Fracture of concrete specimens at the 28-day split tensile test: (a) Control, (b) C−1, (c) C−3, and (d) C−5.

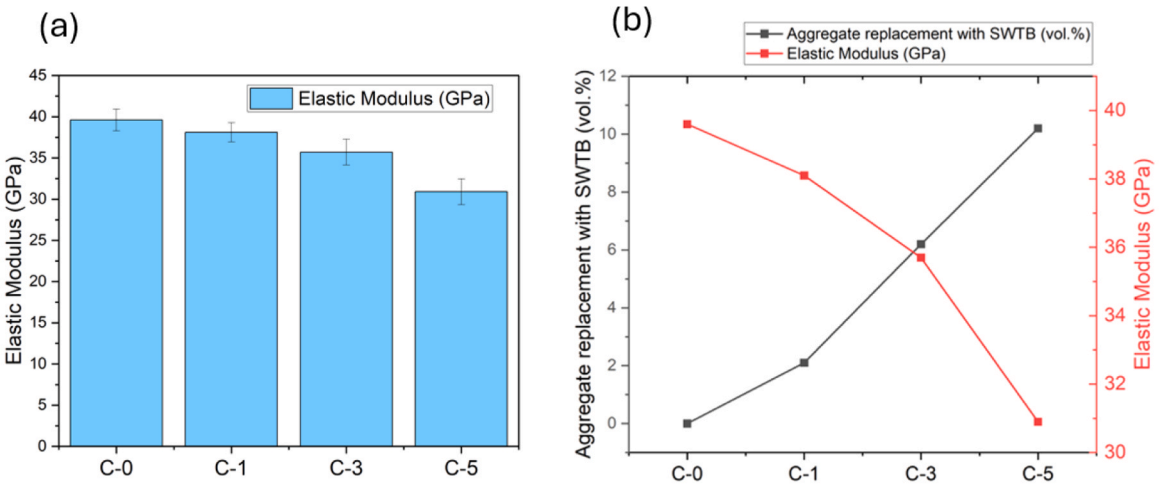

Fig. 13. Elastic modulus results of concrete specimens: (a) measured elastic modulus values for C−0, C−1, C−3, and C−5 mixtures; (b) relationship between SWTB aggregate replacement level (vol%) and elastic modulus.

illustrated in Fig. 11. The results at 7 days showed no significant variation between the SWTB-containing mixtures and the control sample. However, the effects of SWTB incorporation became more pronounced in the 28-day tests. This can be attributed to the continued hydration process, which enhances the interaction between the SWTB fibers and the concrete matrix over time, thereby strengthening the fiber–matrix bond.

At 28 days, the control mixture reached a split tensile strength (f_{ct}) of 4.27 MPa, while the SWTB mixtures showed slightly lower values of 3.6 MPa (C−1), 3.8 MPa (C−2), and 3.9 MPa (C−5). Although the incorporation of SWTB reduced tensile strength relative to the control, a gradual increase was observed within the SWTB series as the SWTB dosage and therefore the fiber content increased. This suggests that the reinforcing action of the embedded fibers progressively mitigated the negative influence of SWTB on tensile performance. Even though the reference sample exhibited the highest strength, its failure mode was more brittle, resulting in the specimen fracturing into two distinct pieces. The fracture patterns of all mixtures are presented in Fig. 12. The contribution of the fibers to mechanical behavior was further evaluated through CMOD and toughness assessment.

3.3.2. *Elastic modulus*

The EMod results of the prepared concrete samples are presented in Fig. 13(a) and Table 10. All mixtures exhibited average EMod values

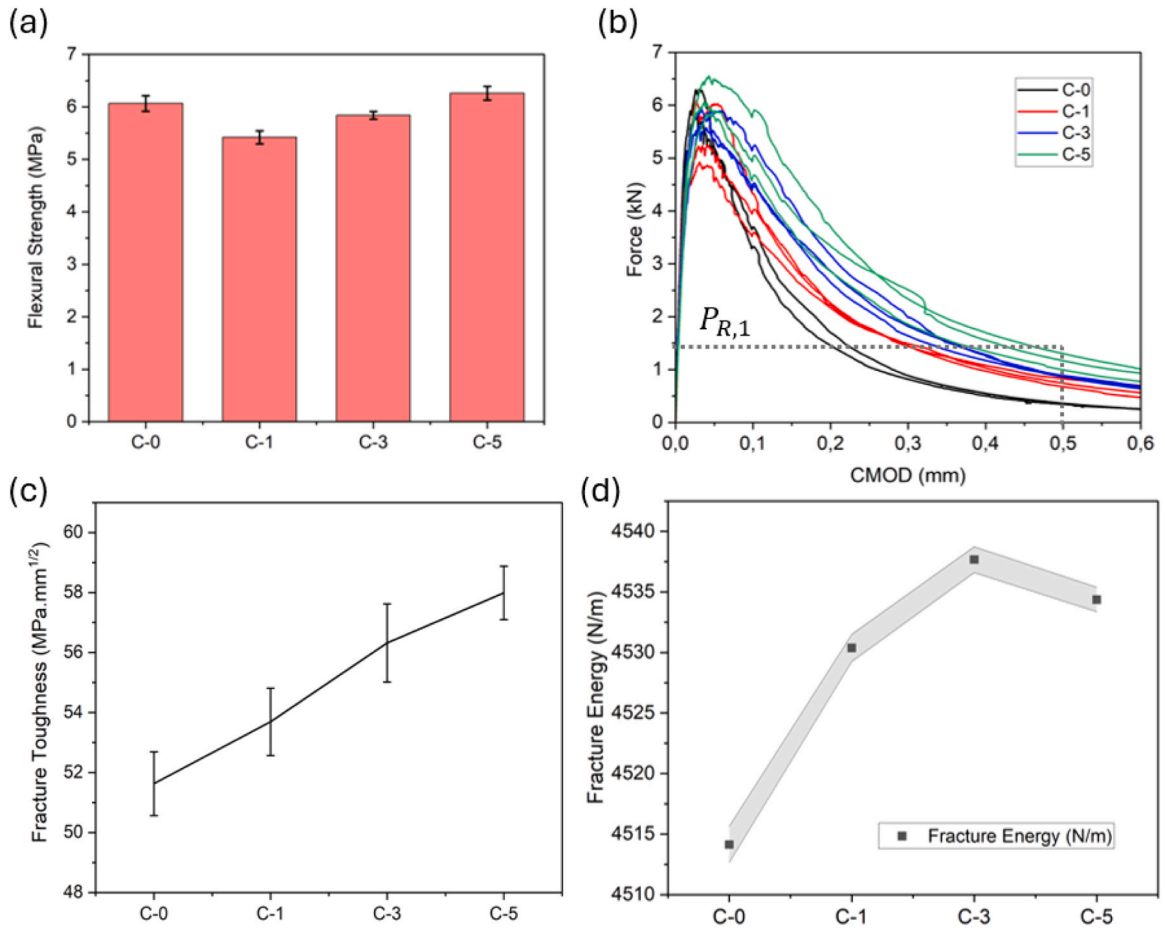

Fig. 14. Fracture properties of the concrete specimens (a) Flexural strength; (b) Load-CMOD curves of concrete beams; (c) Fracture toughness (K_{IC}); (d) Fracture energy (G_f).

exceeding 30 GPa, confirming their suitability for structural applications [64]. However, a clear decreasing trend in elastic modulus is observed with increasing SWTB content, as illustrated in Fig. 13(a), which signifies a reduction in rigidity with higher SWTB dosage. The reference mixture (C−0) recorded the highest modulus at 39.6 GPa, while the C−5 mix showed the lowest value at 30.9 GPa. The data suggests an almost linear decline in modulus: each 1% increase in SWTB replacement corresponds to an approximate reduction of 1.687 GPa in the elastic modulus. This trend aligns closely with findings reported by [64]. The decrease in the elastic modulus can be attributed to the change in the stiffness balance of the composite upon SWTB integration.

It is widely known that replacing natural aggregates with recycled aggregates results in a reduction in the elastic modulus of concrete. This decrease is often more pronounced when the recycled aggregates contain higher proportions of lightweight constituents, such as plastic or rubber contaminants [65]. Fig. 13(b) shows that as the substitution of natural aggregate with SWTB increases, the elastic modulus of the concrete mixtures decreases. This observed trend is consistent with findings reported in the literature. The underlying main reason for this reduction is the substantially lower stiffness of the SWTB, compared to natural river aggregate. Furthermore, the non-granular shape of SWTB particles adversely affect the overall rigidity of concrete [66]. Moreover, the rough and defective surface morphology created by the mechanical shredding process weakens the interfacial transition zone (ITZ). The combination of the lower intrinsic stiffness of SWTB and the impaired ITZ collectively contributes to the observed reduction in the overall rigidity of the concrete.

3.3.3. *Fracture behavior*

The fracture behavior of the specimens was investigated using three-point bending tests on notched beams. The flexural strength results of the concrete mixtures are presented in Table 10 and Fig. 14 (a). For the C−0 mixture, one specimen fractured prior to flexural testing; therefore, the reported flexural strength values for this mixture are based on two valid measurements. As the level of SWTB aggregate replacement increased, a reduction in concrete strength was also reflected in the flexural strength results. The control mixture (C−0) exhibited a flexural strength of 6.0 MPa, while values of 5.4 MPa, 5.8 MPa, and 6.3 MPa were obtained for C−1, C−3, and C−5, respectively. Although an initial decrease in flexural strength was observed with SWTB incorporation, higher SWTB dosages led to an improvement in flexural performance. This enhancement can be attributed to the increased number of macrofibers introduced into the concrete with higher SWTB contents.

The fracture process of the concrete specimens under flexural loading initiates with the formation of a primary crack at the tip of the pre-existing notch. As the applied load increases, this crack progressively propagates toward the loading point, undergoing an initiation phase, deepening, and a pronounced widening of the crack opening. The corresponding load–crack mouth opening displacement (P–CMOD) responses are presented in Fig. 14(b). The multifunctional use of SWTB, naturally influences the elastic modulus and the fracture response of the resulting concrete. As demonstrated by Jiangjiang et al. [67] aggregates play a central role in concrete fracture mechanics, particularly in controlling crack propagation from the notch tip. Because natural aggregates typically exhibit the highest stiffness within the composite, they act as mechanical obstacles that help restrain crack growth. When aggregates with reduced stiffness or elongated, needle-like geometries are

introduced, these particles tend to fracture more easily under stress, which can facilitate crack advancement.

Although the SWTB aggregate fraction has a lower modulus than natural aggregates, the macrofiber fraction within the SWTB waste provides a competing toughening mechanism. The fiber bridging behavior enhances energy absorption during fracture and ultimately governs the material response. This effect is clearly reflected in the P–CMOD curves, where the C−1, C−3, and C−5 mixtures sustain higher loads before failure than the control sample. These results suggest that the reinforcing contribution of the SWTB fibers compensates for, and even surpasses, the potential weakening associated with replacing stiff natural aggregates with lower-stiffness SWTB particles. This improvement is also evident when comparing the residual flexural strengths of the specimens at a CMOD opening of 0.5 mm. The residual tensile strengths were calculated in accordance with the recommended procedures outlined by RILEM [68], and the fib Model Code [69]. When the CMOD reaches 0.5 mm, the corresponding residual flexural strength is denoted as $f_{R,1}$. For beams tested under three-point bending, $f_{R,1}$ is calculated as follows [68,70]:

$$f_{R,1} = \frac{3P_{R,1}L}{2bh_{sp}^{\ 2}} \tag{7}$$

where $P_{R,1}$ is the load corresponding to a CMOD of 0.5 mm, and L and b are the span and the section width of the beam, respectively. For notched beams, h_{sp} is defined as the distance between the notch tip and the top surface of the beam.

The reference mixture (C−0) exhibited an $f_{R,1}$ value of 0.355 MPa. In contrast, the mixtures incorporating SWTB demonstrated significantly higher residual strengths: C−1 reached 0.789 MPa, corresponding to a 122% increase relative to the control; C−3 achieved 0.882 MPa, representing an improvement of approximately 148%; and C−5 attained the highest value, 1.242 MPa, which corresponds to an increase of nearly 250%. These results clearly indicate that higher SWTB dosages substantially enhance the post-cracking load-carrying capacity of the concrete.

Fracture toughness (K_{IC}) is a key material parameter that characterizes a material's resistance to unstable crack propagation under stable strain conditions. Higher K_{IC} values indicate improved resistance to brittle fracture. The fracture toughness is calculated by [71]:

$$K_{IC} = \frac{3(P + \frac{1}{2}mg)}{2bh^2} l_0 \sqrt{\pi a} \times f(a) \tag{8}$$

and

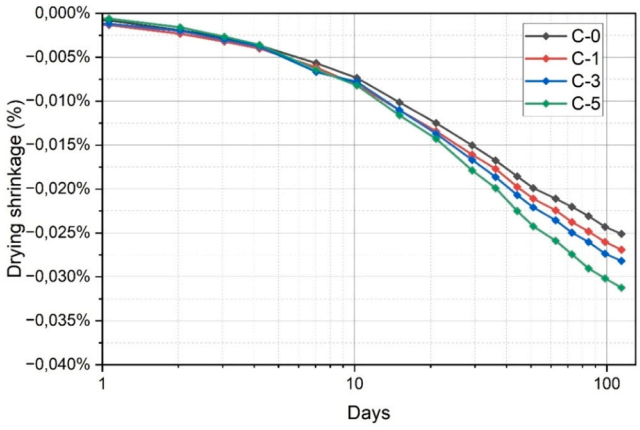

Fig. 15. Drying shrinkage kinetics of concrete prisms depending on SWTB dosage.

$$a = \frac{a + h_0}{h + h_0} \tag{9}$$

where P is the applied load (kN), mg is the beam weight between the supports, l_0 is the span length, a is the crack length, and h_0 is the extensometer blade thickness (1.5 mm), $f(a)$ is a geometric function related to the aspect ratio β and a/h.

In this study, the span/height ratio of our experimental beam is $\beta = 4$. The expression for $f_{\beta=4}(a)$ is given as [72,73]:

$$f_{\beta=4}(a) = \frac{1}{\sqrt{\pi}} \frac{1.99 - a(1-a)(2.15 - 3.93a + 2.7a^2}{(1+2a)(1-a)^{3/2}} \tag{10}$$

The calculated fracture toughness values (MPa.mm$^{1/2}$) are presented in Fig. 14(c). A continuous increase in fracture toughness is observed with increasing SWTB content in concrete. The values rise from 51.2 in the reference mixture (C−0) to 53.6 in C−1, 56.3 in C−3, and 57.8 in C−5. This progressive improvement indicates that the incorporation of SWTB enhances the crack resistance of the concrete, despite the lower stiffness and irregular morphology of the waste material. The trend suggests that the fiber fraction within the SWTB provides an effective toughening contribution as its dosage increases.

Yu et al. [72] indicate recycled wind turbine blade fibers, when cut into a needle-like shape with lengths exceeding 60 mm, significantly enhance the fracture toughness of concrete. In this study, the absence of a steeper increase in fracture toughness can be attributed to the heterogeneous nature of the fiber fraction within the SWTB, the relatively short fiber lengths, and the defects present on the fiber surfaces, which are inherent to the shredding process (Fig. 1). These defects limit the development of strong fiber–matrix bonds. Although the concrete mixtures did not incorporate selectively sorted SWTB fibers for optimized reinforcement, the use of SWTB still produced a positive effect on the fracture toughness of the concrete.

The fracture energy (G_F) can be determined through three-point bending tests on prefabricated notched beams, using the area under the load–deflection (P- δ) curve as the basis for calculation [72,74]. Alternatively, P-CMOD curve may be used for the calculation in order to obtain a more precise estimate of the fracture energy, providing greater robustness against potential influences such as surface roughness, follows from [73]:

$$G_F = \frac{\frac{l_0}{4H}\int Pd(CMOD) + \frac{l_0}{4H} mgCMOD_0}{b(h - a_0)} \tag{11}$$

where l_0 is the distance between the supports, $H = h + h_0$ represents the sum of the beam height and the blade thickness of the fixed-clamp extensometer, and $CMOD_0$ is the maximum crack opening displacement.

The calculated fracture energy values, determined from the area enclosed by the load–CMOD curve up to a crack opening displacement of 0.3 mm, are presented in Fig. 14(d). The results show that the fracture energy remains relatively consistent across all mixtures. The control sample (C−0) reached a fracture energy of 4514.14 N/m, while the SWTB-containing mixtures exhibited values of 4530.38 N/m for C−1, 4537.67 N/m for C−3, and 4534.37 N/m for C−5. These findings indicate that incorporating SWTB does not significantly alter the overall fracture energy of the concrete, with only marginal increases observed as the SWTB content rises.

In this study, SWTB was not selectively sorted to obtain only the fiber fraction for reinforcement; instead, it was incorporated into the concrete as the original waste at dosages of up to 5% of the total concrete mass. This level of incorporation resulted in noticeable differences in mixture density, with higher SWTB dosages leading to a reduction in the overall density of the concrete (Table 9). Since the calculation of fracture energy depends on specimen density, this reduction offsets the toughening effect provided by the SWTB fibers. As a result, the fracture energy values

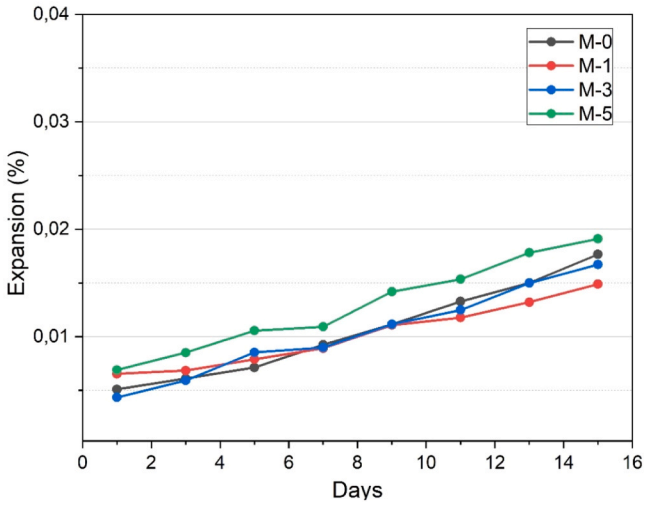

Fig. 16. Expansions during accelerated mortar bar test.

remain almost unchanged across the mixtures.

3.4. Drying shrinkage

Drying shrinkage is associated with the loss of free water from concrete and continues throughout its service life. However, it generally slows down significantly after approximately 91 days, as less water content is available at later ages. Drying shrinkage is influenced by the stiffness of the cementitious matrix. Therefore, the use of fibers may help mitigate shrinkage strains by increasing matrix rigidity [37]. Moreover, the rigidity of coarse aggregates and the elastic modulus of concrete both play an important role in drying shrinkage behavior, with higher stiffness associated with lower shrinkage strains [75]. The literature reports that the use of rubber or plastic originated aggregates in concrete can increase drying shrinkage [76,77].

Fig. 15 presents the drying shrinkage behavior of the different concrete prisms over 120 days on a logarithmic time scale. During the first five days, all concrete specimens exhibited similar shrinkage strains. Subsequently, a relatively small but proportional increase in shrinkage was observed as the SWTB content in the mixtures increased. This rise in shrinkage strain is primarily attributed to the reduced stiffness of the overall matrix, resulting from the replacement of conventional components with SWTB. Additionally, Zhang et al. [75] reported that when aggregates with high water absorption capacity are used, the additional water required to maintain the target water/cement ratio, according to ACI concrete mix design recommendations, may further contribute to drying shrinkage. Accordingly, the relatively higher shrinkage strain observed in the C−5 concrete in this study can be associated with both reduced stiffness of the system and the impact of additional mixing water. Furthermore, the irregular and porous structure of SWTB particles serves as a contributing factor to this increase. Indeed, previous studies have reported that incorporating GFRP wastes into concrete can lead to noticeable increases in drying shrinkage [44,78].

In contrast to reports in the literature, all specimens in this study exhibited relatively low drying shrinkage despite the high levels of SWTB replacement. This outcome is attributed to the particle-packing-based design approach, which enabled the concrete to achieve low porosity and high stiffness. Consequently, all mixtures demonstrated shrinkage strains below 0.035% at 120 days.

3.5. Alkali silica reaction

ASR is a chemical reaction that occurs between the highly alkaline pore solution of cement paste and reactive amorphous silica present in aggregates. This reaction is recognized as a long-term durability concern in concrete systems. The use of glass-containing wastes as aggregate replacements in concrete and mortar, particularly at higher replacement levels, may increase ASR expansion [79,80].

The accelerated mortar bar test results of the specimens prepared in this study are presented in Fig. 16. The expansion values of all specimens are well below the recommended 0.1% limit [60,81]. The mixtures incorporated a relatively high SWTB content, which inherently introduced a significant glass fraction into the concrete. Despite this, no measurable increase in ASR risk was observed, aligning with literature reports on the use of GFRP originated reinforcement in cementitious

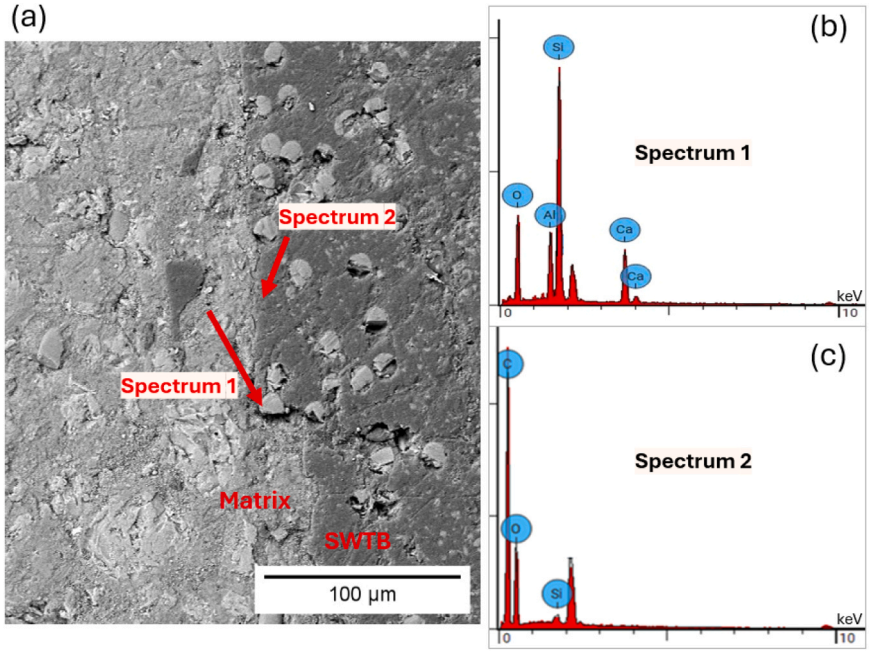

Fig. 17. SEM image of the M−5 mortar after 90 days of the accelerated mortar bar test: (a) mortar matrix with an embedded SWTB particle, (b) EDS analysis of the glass fiber, and (c) EDS analysis of the epoxy resin.

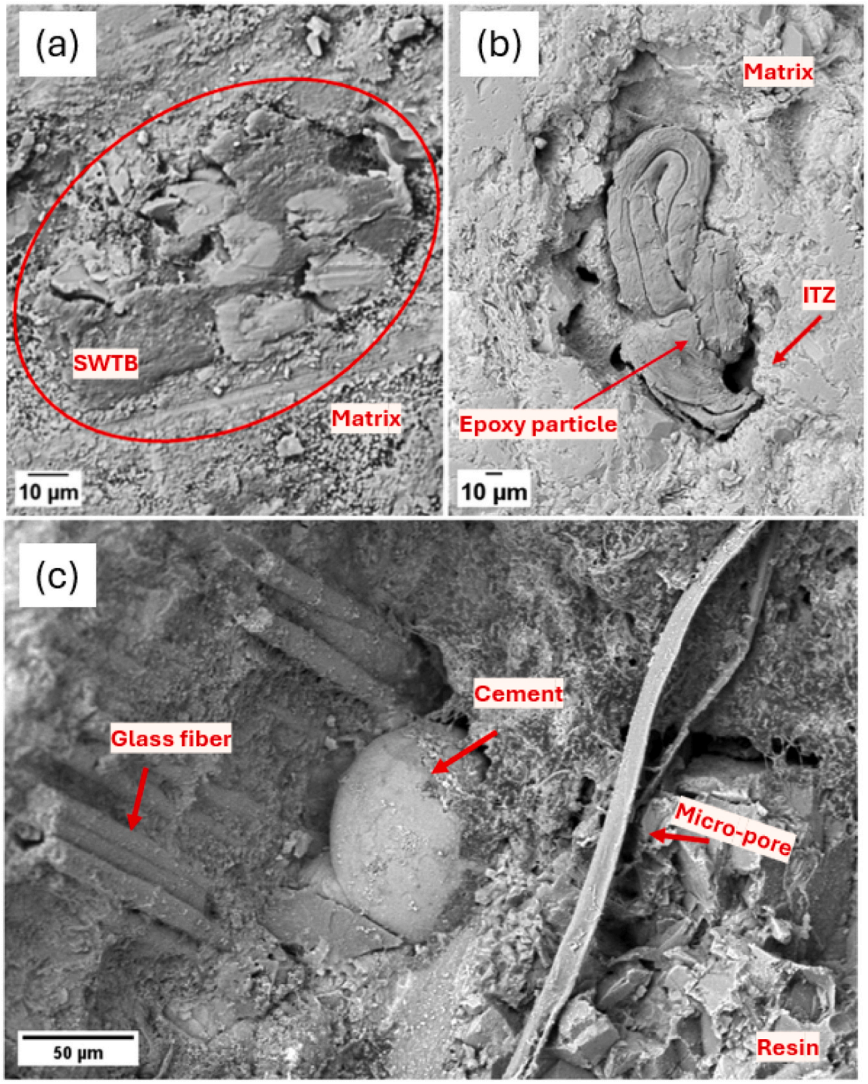

Fig. 18. SEM images of the C−5 concrete specimen showing SWTB particles at different size ranges: (a) cement replacement–sized SWTB with glass fiber residues, (b) cement replacement–sized SWTB without glass fiber residues, and (c) inside of a large SWTB particle used as aggregate replacement in concrete.

composites [44,82,83].

This result can primarily be attributed to the inherent properties of E-glass fibers, which are commonly used in wind turbine blade manufacturing and exhibit high resistance to ASR. Additionally, particle size plays a critical role; the coarser fractions of SWTB have a lower specific surface area, which limits their chemical reactivity. Furthermore, the resin layer surrounding the glass fibers limits their direct contact with the alkaline environment, thereby mitigating the potential for alkali silica reactions [80,84]. The resin part of SWTB may also locally reduce the pH of the pore solution, which can further suppress ASR activity [40].

3.6. Microstructure of mortar and concrete prisms

The micro-structure captured in Fig. 17(a) shows the mortar matrix and an embedded SWTB particle, where darker areas correspond to regions of lower density. Although the M−5 specimen exhibited the highest ASR expansion among all samples, no ASR-related cracking was observed within the mortar. Despite prolonged exposure to a highly alkaline environment, the epoxy phase of SWTB remained stable. The circular features observed within the polymer phase of SWTB correspond to the cross-sections of glass fibers, and no ASR gel formation was detected around these fibers. Fig. 17(b) and Fig. 17(c) present the EDS analyses of the glass fiber and the epoxy resin, respectively. These microstructural observations further support the ASR test results, confirm the limited ASR activity associated with the use of SWTB.

Fig. 18 shows SEM images of the internal microstructure of the C−5 concrete specimen. Fig. 18(a) presents an SWTB particle in the 50–75µm size range used as cement replacement. The particle contains residual glass fiber fragments and surrounding epoxy resin, retains its original morphology, and shows no signs of chemical alteration within the matrix. However, defects resulting from the shredding process locally increased the micro-porosity of the cementitious matrix. Fig. 18(b) presents a resin particle in the 50–100 µm size range without embedded glass fiber fragments. As a natural outcome of the shredding process, SWTB generates particles with random sizes, morphologies, and compositions. The particle shown falls within the cement replacement size range. The resin phase appears stable within the cementitious matrix; however, it introduces local micro-porosity and forms a relatively weak interfacial transition zone (ITZ) with the surrounding matrix. As observed in Fig. 18(a) and (b), the use of SWTB as a cement replacement appears to reduce the stiffness of the cementitious matrix.

Fig. 18(c) presents the internal structure of a relatively large SWTB particle corresponding to the aggregate replacement fraction in concrete. In the image, glass fibers within the SWTB particle are observed to be present together. However, the surrounding polymer layer appears to

be locally disrupted, most likely as a result of the shredding process. Cement grains that penetrated into this region remained unhydrated. In addition, micro-pores and resin-rich regions are also present within the interior of the SWTB particle. The defective structure of SWTB particles used as aggregate replacement is in agreement with the reduction in concrete stiffness observed at higher replacement levels.

4. Conclusions

This study investigated the multifunctional incorporation of non-selective shredded wind turbine blade (SWTB) waste into concrete as a partial cement replacement, aggregate substitute, and fiber reinforcement. Based on the experimental findings and microstructural analyses, the following conclusions can be drawn:

- The research successfully demonstrated that SWTB functions as a multipurpose constituent, characterized by significant size and shape variation (ranging from 0.063 mm powder to 80 mm fibrous flakes). The application of the Modified Andreasen and Andersen (MAA) particle packing model proved essential in accommodating these complex morphological characteristics to achieve a dense concrete skeleton, effectively mitigating the rigidity and strength losses typically associated with high composite waste contents.
- Isothermal calorimetry revealed that the partial replacement of cement with SWTB powder (up to 2.5% by mass) does not exert a retarding effect on the hydration process. The stability of the setting times suggests that the epoxy residues within the waste do not chemically interfere with the cementitious reactions.
- Despite the simultaneous replacement of up to 10.2% aggregate and 4.4% cement by volume, the concrete mixtures maintained structural-grade performance with 28-day compressive strengths exceeding 45 MPa. The reduction in elastic modulus was found to be linear with increasing SWTB dosage, attributed to the lower stiffness of the resinous phase compared to natural river aggregates.
- The integration of SWTB enhanced the post-cracking behavior of the concrete. The fibrous fraction provided an effective bridging mechanism, leading to a residual flexural strength increase of up to 250% at a CMOD of 0.5 mm. The mechanical shredding process introduces surface defects and morphological irregularities to the SWTB particles, which may limit the full potential of fiber-matrix bonding, yet the results demonstrate a significant improvement in energy absorption during fracture.
- Accelerated mortar bar tests and SEM-EDS examinations confirmed that SWTB does not pose an alkali-silica reaction (ASR) risk. The protective epoxy resin coating on the glass fibers effectively limits direct exposure to the alkaline pore solution, ensuring the long-term chemical stability of the composite.
- To the best of the authors' knowledge, this study achieves a unique integration of high SWTB substitution levels (comprising 10.2% aggregate substitute, 4.4% cement replacement, and 2.6% fiber reinforcement together by volume) while successfully retaining structural-grade performance (45 MPa compressive strength, 30 GPa elastic modulus, and improved fracture performance). At these high dosages, the concrete also exhibited no measurable ASR risk or excessive drying shrinkage, a combination of findings that has not been previously reported in the literature.

CRediT authorship contribution statement

Gauvin Florent: Writing – review & editing, Methodology. **Lushnikova Nataliya:** Writing – review & editing, Investigation. **H.J.H Brouwers:** Writing – review & editing, Supervision, Funding acquisition. **Chevalier Maelle:** Visualization, Software, Investigation. **Duyal Ceren:** Writing – original draft, Visualization, Validation, Software, Methodology, Investigation, Data curation, Conceptualization.

Declaration of Competing Interest

The authors declare that they have no known competing financial interests or personal relationships that could have appeared to influence the work reported in this paper.

Acknowledgment

This work was supported by the European Union's Horizon Europe Research and Innovation Programme under grant agreement no. 101096437 (Blades2Build). Funded by the European Union. Views and opinions expressed are however, those of the author(s) only and do not necessarily reflect those of the European Union or the European Climate, Infrastructure and Environment Executive Agency (CINEA). Neither the European Union nor the granting authority can be held responsible.

The authors would like to thank Beatrice Cerrai for her technical support and expertise during the SEM analysis.

During the preparation of this work, the authors used Gemini in order to improve readability, grammar, and language. After using this tool/service, the authors reviewed and edited the content as needed and took full responsibility for the content of the publication.

Appendix A

Nomenclature

SWTB	Shredded wind turbine blade
D_{max}	Maximum particle size
D_{min}	Minimum particle size
PSD	Particle size distribution
q	Distribution modulus
MAA model	Modified Andreasen & Andersen model
RSS	Residual sum of squares
R^2	Coefficient of determination
P_{target}	Target curve
P_{mix}	Mix curve

(*continued on next page*)

(*continued*)

E	Secant modulus of elasticity
CMOD	Crack mouth opening displacement
P	Test beam load
P_{max}	Test beam maximum load
l_0	Net span of the test beam
α	Crack length of test beam
h_0	Blade thickness of the fixed clamp extensometer
β	Span-to height ratio
h	Test beam height
$f(\alpha)$	Shaped function related to β and α/h
f_c	Compressive strength
f_{ct}	Splitting tensile strength
f_p	Flexural strength
f_R	Residual flexural tensile strength
$f_{R,1}$	Residual flexural tensile strength (at CMOD = 0.5 mm)
G_F	Fracture energy
K_{IC}	Fracture toughness
σ	Stress
ϵ	Strain

Appendix B

The residual sum of squares (RSS) is calculated by:

$$RSS = \sum_{i=1}^{n} \left(P_{mix}\left(D_i^{i+1}\right) - P_{target}\left(D_i^{i+1}\right)\right)^2 \tag{B.1}$$

The coefficient of determination (R^2), which quantifies the fitting degree between the target and actual packing curves, is calculated by:

$$R^2 = 1 - \frac{RSS}{\left(\sum_{i=1}^{n}\left(P_{mix}\left(D_i^{i+1}\right) - \overline{P_{mix}}\right)\right)^2} \tag{B.2}$$

Where $\overline{P_{mix}}$ corresponds to the overall average of the particle size distribution and calculated as follows:

$$\overline{P_{mix}} = \frac{1}{n}\sum_{i=1}^{n} P_{mix}\left(D_i^{i+1}\right) \tag{B.3}$$

Data availability

Data will be made available on request.

References

[1] S. Griffiths, B.K. Sovacool, D.D.F. Del Rio, A.M. Foley, M.D. Bazilian, J. Kim, J. M. Uratani, Decarbonizing the cement and concrete industry: a systematic review of socio-technical systems, technological innovations, and policy options, Renew. Sustain. Energy Rev. 180 (2023) 113291, https://doi.org/10.1016/j.rser.2023.113291.

[2] X. Song, K. An, R. Wang, G. Liu, C. Wang, Toward net-zero cement: linking demand-side measures with plant-level technology strategies, Resour. Conserv. Recycl. 220 (2025) 108339, https://doi.org/10.1016/j.resconrec.2025.108339.

[3] O.F.A. Perez, D.R. Florez, L.M.Z. Vergara, K.V.H. Benavides, Innovative use of agro-waste cane bagasse ash and waste glass as cement replacement for green concrete. Cost analysis and carbon dioxide emissions, J. Clean. Prod. 379 (2022) 134822, https://doi.org/10.1016/j.jclepro.2022.134822.

[4] S.A. Miller, V.M. John, S.A. Pacca, A. Horvath, Carbon dioxide reduction potential in the global cement industry by 2050, Cem. Concr. Res. 114 (2018) 115–124, https://doi.org/10.1016/j.cemconres.2017.08.026.

[5] R.M. Andrew, Global CO2 emissions from cement production, 1928-2018, Earth Syst. Sci. Data 11 (4) (2019) 1675–1710, https://doi.org/10.5194/essd-11-1675-2019.

[6] Y. Gao, F. Zou, S. Wang, H. Sui, J. Yu, B. Xu, W. Chen, Y. Liu, Redefining the cement substitution potential of recycled concrete powder using graphene oxide coating, Cem. Concr. Compos. 164 (2025) 106276, https://doi.org/10.1016/j.cemconcomp.2025.106276.

[7] B. Wang, L. Yan, Q. Fu, B. Kasal, A comprehensive review on recycled aggregate and recycled aggregate concrete, Resour. Conserv. Recycl. 171 (2021) 105565, https://doi.org/10.1016/j.resconrec.2021.105565.

[8] L. Wu, Z. Sun, Y. Cao, Modification of recycled aggregate and conservation and application of recycled aggregate concrete: A review, Constr. Build. Mater. 431 (2024) 136567, https://doi.org/10.1016/j.conbuildmat.2024.136567.

[9] E. Aprianti, A huge number of artificial waste material can be supplementary cementitious material (SCM) for concrete production – a review part II, J. Clean. Prod. 142 (2017) 4178–4194, https://doi.org/10.1016/j.jclepro.2015.12.115.

[10] C. Pellegrino, F. Faleschini, C. Meyer, Recycled materials in concrete, Dev. Formul. Reinf. Concr. (2019) 19–54, https://doi.org/10.1016/B978-0-08-102616-8.00002-2.

[11] M.J. Islam, M. Shahjalal, N.M.A. Haque, Mechanical and durability properties of concrete with recycled polypropylene waste plastic as a partial replacement of coarse aggregate, J. Build. Eng. 54 (2022) 104597, https://doi.org/10.1016/j.jobe.2022.104597.

[12] S.A. Yıldızel, Y.O. Özkılıç, A. Bahrami, C. Aksoylu, B. Başaran, A. Hakamy, M. H. Arslan, Experimental investigation and analytical prediction of flexural

behaviour of reinforced concrete beams with steel fibres extracted from waste tyres, Case Stud. Constr. Mater. 19 (2023) e02227, https://doi.org/10.1016/j.cscm.2023.e02227.
[13] J.C.O. Zepper, S.R. van der Laan, K. Schollbach, H.J.H. Brouwers, A Bogue approach applied to basic oxygen furnace slag, Cem. Concr. Res. 175 (2024) 107344, https://doi.org/10.1016/j.cemconres.2023.107344.
[14] A. Taha, W. Alnahhal, Synergistic effects of recycled concrete powder, GGBFS, and basalt fibers on mechanical and durability performance of recycled aggregate concrete, Structures 71 (2025) 108058, https://doi.org/10.1016/j.istruc.2024.108058.
[15] A. Cooperman, A. Eberle, E. Lantz, Wind turbine blade material in the United States: quantities, costs, and end-of-life options, Resour. Conserv. Recycl. 168 (2021) 105439, https://doi.org/10.1016/j.resconrec.2021.105439.
[16] P. Asokan, M. Osmani, A.D.F. Price, Assessing the recycling potential of glass fibre reinforced plastic waste in concrete and cement composites, J. Clean. Prod. 17 (9) (2009) 821–829, https://doi.org/10.1016/j.jclepro.2008.12.004.
[17] J. Beauson, B. Madsen, C. Toncelli, P. Brøndsted, J.I. Bech, Recycling of shredded composites from wind turbine blades in new thermoset polymer composites, Compos. Part A Appl. Sci. Manuf. 90 (2016) 390–399, https://doi.org/10.1016/j.compositesa.2016.07.009.
[18] P. Liu, C.Y. Barlow, Wind turbine blade waste in 2050, Waste Manag. 62 (2017) 229–240, https://doi.org/10.1016/j.wasman.2017.02.007.
[19] A. Tyurkay, G.M. Kirkelund, A.T. Lima, State-of-the-art circular economy practices for end-of-life wind turbine blades for use in the construction industry, Sustain. Prod. Consum. 47 (2024) 17–36, https://doi.org/10.1016/j.spc.2024.03.018.
[20] M. Rani, P. Choudhary, V. Krishnan, S. Zafar, A review on recycling and reuse methods for carbon fiber/glass fiber composites waste from wind turbine blades, Compos. Part B Eng. 215 (2021) 108768, https://doi.org/10.1016/j.compositesb.2021.108768.
[21] M. Modestou, D. Semitekolos, T. Liu, C. Podara, S. Orfanidis, A.T.M. Lima, C. Charitidis, Recycling of glass fibers from wind turbine blade wastes via chemical-assisted solvolysis, Fibers 13 (163) (2025) https://doi.org/10.3390/.
[22] A. Yazdanbakhsh, L.C. Bank, A critical review of research on reuse of mechanically recycled FRP production and end-of-life waste for construction, Polymers 6 (6) (2014) 1810–1826, https://doi.org/10.3390/polym6061810.
[23] S.H. Mamanpush, H. Li, K. Englund, A.T. Tabatabaei, Recycled wind turbine blades as a feedstock for second generation composites, Waste Manag. 76 (2018) 708–714, https://doi.org/10.1016/j.wasman.2018.02.050.
[24] T. Liu, C. Paraskevoulakos, U.A. Mughal, A. Tyurkay, N. Lushnikova, H. Song, C. Duyal, S. Tumkur-Karnick, F. Gauvin, A.T. Lima, Mechanisms and applications of wind turbine blade waste in cementitious composites: a review, Mater. & Des. 251 (2025) 113732, https://doi.org/10.1016/j.matdes.2025.113732.
[25] D. Baturkin, O.A. Hisseine, R. Masmoudi, A. Tagnit-Hamou, L. Massicotte, Valorization of recycled FRP materials from wind turbine blades in concrete, Resour. Conserv. Recycl. 174 (2021) 105807, https://doi.org/10.1016/j.resconrec.2021.105807.
[26] A. Yazdanbakhsh, L.C. Bank, K.A. Rieder, Y. Tian, C. Chen, Concrete with discrete slender elements from mechanically recycled wind turbine blades, Resour. Conserv. Recycl. 128 (2018) 11–21, https://doi.org/10.1016/j.resconrec.2017.08.005.
[27] M. Hofmeister, Recycling turbine blade composites: Concrete aggregate and reinforcement, Wind Energy Sci. Eng. Policy Symp Proc. (2012).
[28] V. Revilla-Cuesta, A.B. Espinosa, R. Serrano-López, M. Skaf, J.M. Manso, Mechanical properties of concrete mixes with selectively crushed wind turbine blade: comparison with raw-crushing, Materials 17 (24) (2024) 6299, https://doi.org/10.3390/ma17246299.
[29] B. Fu, K.C. Liu, J.F. Chen, J.G. Teng, Concrete reinforced with macro fibres recycled from waste GFRP, Constr. Build. Mater. 310 (2021) 125063, https://doi.org/10.1016/j.conbuildmat.2021.125063.
[30] G.T. Xu, M.J. Liu, Y. Xiang, B. Fu, Valorization of macro fibers recycled from decommissioned turbine blades as discrete reinforcement in concrete, J. Clean. Prod. 379 (2022) 134550, https://doi.org/10.1016/j.jclepro.2022.134550.
[31] T. Zhao, Y. Lv, J. Chen, P. Song, M. Sun, X. Zhang, L. Huang, Effect of glass fiber-reinforced plastic waste on the mechanical properties of concrete and evaluation of its feasibility for reuse in concrete applications, Materials 16 (20) (2023) 6772, https://doi.org/10.3390/ma16206772.
[32] V. Revilla-Cuesta, M. Skaf, V. Ortega-López, J.M. Manso, Raw-crushed wind-turbine blade: waste characterization and suitability for use in concrete production, Resour. Conserv. Recycl. 198 (2023) 107160, https://doi.org/10.1016/j.resconrec.2023.107160.
[33] B. Zhou, M. Zhang, L. Wang, G. Ma, Experimental study on mechanical property and microstructure of cement mortar reinforced with elaborately recycled GFRP fiber, Cem. Concr. Compos. 117 (2021) 103908, https://doi.org/10.1016/j.cemconcomp.2020.103908.
[34] T. Liu, H. Reascos, U.A. Mughal, G.M. Kirkelund, A.T. Lima, Improving mortar properties with waste wind turbine blade fibers and superplasticizer, Constr. Build. Mater. 472 (2025) 140864, https://doi.org/10.1016/j.conbuildmat.2025.140864.
[35] V. Ortega-López, F. Faleschini, N. Hurtado-Alonso, J. Manso-Morato, V. Revilla-Cuesta, Analysis of raw-crushed wind-turbine blade as an overall concrete addition: stress–strain and deflection performance effects, Compos. Struct. 340 (2024) 118170, https://doi.org/10.1016/j.compstruct.2024.118170.
[36] T. Liu, C. Paraskevoulakos, A.T. Lima, Mitigation of Alkali-Silica Reaction by Shredded Wind Turbine Blade Waste in Mortar. Second RILEM ICEC, Springer, 2024, pp. 504–514, https://doi.org/10.1007/978-3-031-62690-6_52.
[37] V. Revilla-Cuesta, M. Skaf, J. Manso-Morato, N. Hurtado-Alonso, J.M. Manso, Deepening the effect of selectively crushed wind-turbine blade on the dimensional stability and high-temperature resistance of concrete, J. Build. Eng. 111 (2025) 113440, https://doi.org/10.1016/j.jobe.2025.113440.
[38] J.R. Correia, N.M. Almeida, J.R. Figueira, Recycling of FRP composites: reusing fine GFRP waste in concrete mixtures, J. Clean. Prod. 19 (15) (2011) 1745–1753, https://doi.org/10.1016/j.jclepro.2011.05.018.
[39] P.S. Oliveira, M.L.P. Antunes, N.C. da Cruz, E.C. Rangel, A.R.G. de Azevedo, S. F. Durrant, Use of waste collected from wind turbine blade production as an eco-friendly ingredient in mortars for civil construction, J. Clean. Prod. 274 (2020) 122948, https://doi.org/10.1016/j.jclepro.2020.122948.
[40] T. Liu, C. Duyal, C. Paraskevoulakos, K. Enemark-Rasmussen, A.T. Lima, Effect of wind turbine blade waste on cement hydration and gel structure: competitive interaction of glass and polyester resin, Compos. Part B Eng. 311 (2026) 113273, https://doi.org/10.1016/j.compositesb.2025.113273.
[41] R. Yu, P. Spiesz, H.J.H. Brouwers, Mix design and properties assessment of ultra-high performance fibre reinforced concrete (UHPFRC), Cem. Concr. Res. 56 (2014) 29–39, https://doi.org/10.1016/j.cemconres.2013.11.002.
[42] R. Yu, P. Spiesz, H.J.H. Brouwers, Static properties and impact resistance of a green Ultra-High Performance Hybrid Fibre Reinforced Concrete (UHPHFRC): experiments and modeling, Constr. Build. Mater. 68 (2014) 158–171, https://doi.org/10.1016/j.conbuildmat.2014.06.033.
[43] P.P. Li, Q.L. Yu, H.J.H. Brouwers, W. Chen, Conceptual design and performance evaluation of two-stage ultra-low binder ultra-high performance concrete, Cem. Concr. Res. 125 (2019) 105858, https://doi.org/10.1016/j.cemconres.2019.105858.
[44] A. Dehghan, K. Peterson, A. Shvarzman, Recycled glass fiber reinforced polymer additions to Portland cement concrete, Constr. Build. Mater. 146 (2017) 238–250, https://doi.org/10.1016/j.conbuildmat.2017.04.011.
[45] EN 933-2, Tests for Geometrical Properties of Aggregates - Part 2: Determination of Particle Size Distribution -Test Sieves, Nominal Size Apertures (1996).
[46] EN 1097-6, Tests for Mechanical and Physical Properties of Aggregates - Part 6: Determination of Particle Density and Water Absorption, 2013.
[47] X. Zhao, D. Pakula, M. Frydrych, B. Sztorch, R. Kozera, H. Liu, H. Zhou, R. E. Przekop, Treatment and valorization of waste wind turbines: component identification and analysis, Materials 18 (2) (2025) 468, https://doi.org/10.3390/ma18020468.
[48] ACI Committee 211.1-91, Standard Practice for Selecting Proportions for Normal, Heavyweight, and Mass Concrete, American Concrete Institute, Farmington Hills, 1991.
[49] M. Hunger, An integral design concept for ecological self-compacting concrete, Eindhoven University of Technology, Netherlands, 2010.
[50] G. Hüsken, H.J.H. Brouwers, A new mix design concept for earth-moist concrete: a theoretical and experimental study, Cem. Concr. Res. 38 (10) (2008) 1246–1259, https://doi.org/10.1016/j.cemconres.2008.04.002.
[51] G. Hüsken, A multifunctional design approach for sustainable concrete: with application to concrete mass products, Eindhoven University of Technology, Netherlands, 2010.
[52] ASTM C 1609, Flexural Performance of Fiber-Reinforced Concrete (Using Beam with Third-Point Loading), ASTM International, 2012.
[53] ASTM C143/C143M, Standard Test Method for Slump of Hydraulic-Cement Concrete, ASTM International, 2012.
[54] EN 12390-2, Testing Hardened Concrete - Part 2: Making and Curing Specimens for Strength Tests, 2019.
[55] EN 12390-3, Testing Hardened Concrete - Part 3: Compressive Strength of Test Specimens, 2019.
[56] EN 12390-6, Testing Hardened Concrete. Tensile Splitting Strength of Test Specimens, 2009.
[57] EN 14651, Test method for metallic fibre concrete - Measuring the Flexural Tensile Strength (Limit of Proportionality (LOP), Residual), 2007.
[58] EN 12390-13, Testing hardened concrete - Part 13: Determination of Secant Modulus Of Elasticity in Compression, 2013.
[59] EN 12390-16, Testing Hardened Concrete - Part 16: Determination of the Shrinkage of Concrete, 2019.
[60] ASTM C1260, Standard Test Method for Potential Alkali Reactivity of Aggregates (Mortar-Bar Method), ASTM International, 2014.
[61] A. Baranyi, K. Kopecskó, L. Csetényi, Assessing setting times of cementitious materials using semi-adiabatic calorimetry, J. Therm. Anal. Calorim. 149 (17) (2024) 9193–9201, https://doi.org/10.1007/s10973-024-13375-2.
[62] M. Zhang, H. Li, M. Na, B. Zhou, J. Zhang, Improving dispersion of recycled GFRP fiber in cement mortar with sodium hexametaphosphate, Cem. Concr. Compos. 143 (2023) 105232, https://doi.org/10.1016/j.cemconcomp.2023.105232.
[63] F.F. Gao, S.Y. Duan, W.Da Wang, Y.L. Shi, Mechanical properties and microscopic mechanism of concrete incorporation of recycled GFRP fiber with different sizes recovered from ex-service wind turbine blades, Constr. Build. Mater. 491 (2025) 142833, https://doi.org/10.1016/j.conbuildmat.2025.142833.
[64] J. Manso-Morato, N. Hurtado-Alonso, V. Revilla-Cuesta, V. Ortega-López, Management of wind-turbine blade waste as high-content concrete addition: Mechanical performance evaluation and life cycle assessment, Journal of Environmental Management, 373, 123995. https://doi.org/10.1016/j.jenvman.2024.123995.
[65] R.V. Silva, J. De Brito, R.K. Dhir, Establishing a relationship between modulus of elasticity and compressive strength of recycled aggregate concrete, J. Clean. Prod. 112 (2016) 2171–2186, https://doi.org/10.1016/j.jclepro.2015.10.064.
[66] A.S. Dastgerdi, R.J. Peterman, K. Riding, B.T. Beck, Effect of concrete mixture components, proportioning, and compressive strength on fracture parameters, Constr. Build. Mater. 206 (2019) 179–192, https://doi.org/10.1016/j.conbuildmat.2019.02.025.

[67] Y. Jiangjiang, L. Guodong, R. Zhengyi, Z. Wei, T. Jiangqi, Z. Li, S. Xiaolong, Z. Zhimeng, Mixed-mode I-II mesoscale fracture behavior of concrete determined by the realistic aggregate numerical model, Constr. Build. Mater. 226 (2019) 802–817, https://doi.org/10.1016/j.conbuildmat.2019.07.231.
[68] L. Vandewalle, RILEM TC 162-TDF, on Test and Design Methods for Steel Fibre Reinforced Concrete-Background and Experiences, 31, RILEM Publications, 2003.
[69] L. Taerwe, S. Matthys, Fib Model Code for Concrete Structures 2010, Ernst & Sohn, Wiley, 2013.
[70] T. Almusallam, S.M. Ibrahim, Y. Al-Salloum, A. Abadel, H. Abbas, Analytical and experimental investigations on the fracture behavior of hybrid fiber reinforced concrete, Cem. Concr. Compos. 74 (2013) 201–217, https://doi.org/10.1016/j.cemconcomp.2016.10.002.
[71] S.P. Shah, Size-effect method for determining fracture energy and process zone size of concrete, Mater. Struct. 23 (6) (1990) 461–465.
[72] T. Yu, C. Zhou, L. Cao, Y. Zhang, P. Cao, F. Shi, Effect of GFRP fibres recovered from decommissioned wind turbine blades on the fracture properties of concrete, Constr. Build. Mater. 463 (2025) 140121, https://doi.org/10.1016/j.conbuildmat.2025.140121.
[73] J. He, H. Wang, Q. Yu, Flexural fracture behavior of ultra-high performance concrete after high-temperature exposure, Constr. Build. Mater. 481 (2025) 141544.
[74] J. Shi, Y. Lu, R. Zhu, Y. Liu, Y. Zhang, Q. Lv, Experimental evaluation of fracture toughness of basalt macro fiber reinforced high performance lightweight aggregate concrete, Constr. Build. Mater. 411 (2024) 134638, https://doi.org/10.1016/j.conbuildmat.2023.134638.
[75] W. Zhang, M. Zakaria, Y. Hama, Influence of aggregate materials characteristics on the drying shrinkage properties of mortar and concrete, Constr. Build. Mater. 49 (2013) 500–510, https://doi.org/10.1016/j.conbuildmat.2013.08.069.
[76] W.C. Tang, Y. Lo, A. Nadeem, Mechanical and drying shrinkage properties of structural-graded polystyrene aggregate concrete, Cement and Concrete Composites, 30(5), 403-409. https://doi.org/10.1016/j.cemconcomp.2008.01.002.
[77] P. Sukontasukkul, K. Tiamlom, Expansion under water and drying shrinkage of rubberized concrete mixed with crumb rubber with different size, Constr. Build. Mater. 29 (2012) 520–526, https://doi.org/10.1016/j.conbuildmat.2011.07.032.
[78] N. Hurtado-Alonso, M. Bravo, J. de Brito, V. Revilla-Cuesta, M. Skaf, Evaluation of the durability of structural concrete with low contents of Raw-Crushed Wind Turbine Blade, Constr. Build. Mater. 485 (2025) 141900, https://doi.org/10.1016/j.conbuildmat.2025.141900.
[79] A. Saccani, M.C. Bignozzi, ASR expansion behavior of recycled glass fine aggregates in concrete, Cem. Concr. Res. 40 (4) (2010) 531–536, https://doi.org/10.1016/j.cemconres.2009.09.003.
[80] S.C. Paul, B. Šavija, A.J. Babafemi, A comprehensive review on mechanical and durability properties of cement-based materials containing waste recycled glass, J. Clean. Prod. 198 (2018) 891–906, https://doi.org/10.1016/j.jclepro.2018.07.095.
[81] A. Shayan, H. Morris, A comparison of RTA T363 and ASTM C1260 accelerated mortar bar test methods for detecting reactive aggregates, Cem. Concr. Res. 31 (4) (2001) 655–663, https://doi.org/10.1016/S0008-8846(00)00491-9.
[82] D. García, I. Vegas, I. Cacho, Mechanical recycling of GFRP waste as short-fiber reinforcements in microconcrete, Constr. Build. Mater. 64 (2014) 293–300, https://doi.org/10.1016/j.conbuildmat.2014.02.068.
[83] H. Rodin III, S. Nassiri, K. Englund, O. Fakron, H. Li, Recycled glass fiber reinforced polymer composites incorporated in mortar for improved mechanical performance, Constr. Build. Mater. 187 (2018) 738–751, https://doi.org/10.1016/j.conbuildmat.2018.07.169.
[84] M.W. Kaboré, D. Perrin, R. Idir, P. Ienny, É. Garcia-Diaz, Y. El Bitouri, A review on the valorization of recycled glass fiber-reinforced polymer (rGFRP) in mortar and concrete: a sustainable alternative to landfilling, Polymers 17 (19) (2025) 2664, https://doi.org/10.3390/polym17192664.